Catena 152 (2017) 115–134

Contents lists available at ScienceDirect

Catena

journal homepage: www.elsevier.com/locate/catena

Unravelling fluvial deposition and pedogenesis in ephemeral stream deposits in the vicinity of the prehistoric rock shelter of Ifri n'Ammar (NE Morocco) during the last 100 ka

Melanie Bartz [a,*], Gilles Rixhon [a], Martin Kehl [a], Meriam El Ouahabi [b], Nicole Klasen [a], Dominik Brill [a], Gerd-Christian Weniger [c], Abdeslam Mikdad [d], Helmut Brückner [a,*]

[a] Institute of Geography, University of Cologne, Albertus-Magnus-Platz, 50923 Cologne, Germany
[b] U. R. Argiles, Géochimie et Environnements sédimentaires, Department of Geology, University of Liège, Place du 20 Août 7, 4000 Liège, Belgium
[c] Neanderthal Museum, Talstraße 300, 40822 Mettmann, Germany
[d] Institut National des Sciences de l'Archéologie et du Patrimoine (INSAP), 1, rue Ghandi, Rabat, Morocco

ARTICLE INFO

Article history:
Received 25 February 2016
Received in revised form 8 November 2016
Accepted 8 December 2016
Available online 17 January 2017

Keywords:
Morocco
Environmental change
Luminescence dating
Micromorphology
Soil formation
Human occupation

ABSTRACT

Our study focuses on the ephemeral stream deposits of Wadi Selloum to identify phases of morphodynamic stability (pedogenesis) and activity (flooding) in the direct vicinity of the rock shelter of Ifri n'Ammar (NE Morocco). As one of the oldest settlement sites of anatomically modern humans (AMH) in North Africa, Ifri n'Ammar documents periodical occupations since ~170 ka. Since the discontinuous settlement record may reflect climate forcing with subsequent landscape changes, we aim at reconstructing the palaeoenvironmental variability recorded in the ephemeral stream deposits. In addition to the use of micromorphological, sedimentological, geochemical and mineralogical methods, the geochronological framework of ephemeral stream deposits was established by the application of different luminescence dating techniques.

The deposition ages between 102 ± 8 ka and 1.3 ± 0.2 ka span different morphodynamically stable and active phases. Periods of enhanced aggradation occurred around ~100 ka, ~75 ka, ~55 ka, after the LGM, and during the Holocene, whilst sedimentation ended after ~1.3 ka. The Wadi Selloum might be characterised by enhanced flooding during humid phases. Pedogenesis may be used as environmental indicator for more humid climate conditions during MIS 3 (palaeo-Calcisol), the early Holocene (Calcisol) and the late Holocene (Fluvisol). This study thus provides first insights into the palaeoenvironmental changes around the rock shelter of Ifri n'Ammar during the last glacial-interglacial cycle.

1. Introduction

Located in NE Morocco, the rock shelter of Ifri n'Ammar represents a key settlement site for anatomically modern humans (AMH) in North Africa. It exhibits discontinuous occupation phases since ~170 ka and therefore records one of the oldest evidence of AMH presence in this region (Nami and Moser, 2010; Richter et al., 2010). It has been shown that climate forcing has affected human settlements in Northern Morocco since the Last Glacial Maximum (LGM; e.g. Barton et al., 2005; Courty and Vallverdu, 2001; Linstädter et al., 2012; Lubell, 2001; Zielhofer and Linstädter, 2006). Numerous investigations on fluvial archives also unravelled palaeoenvironmental conditions during the Late Glacial and the Holocene in the Western Mediterranean (e.g. Barathon et al., 2000; Benito et al., 2015; El Amrani et al., 2008; Ibouhouten et al., 2010; Pissart and Boumeaza, 2010; Wolf and Faust, 2015; Zielhofer et al., 2008, 2010). In contrast, very little information was obtained on geo-archives predating the LGM in NE Morocco (Rixhon et al., 2017).

Against this background, we have investigated the ephemeral stream deposits of the Wadi Selloum at the footslope of the archaeological site of Ifri n'Ammar as this environment exhibits fluvial archives (at least) as old as the marine isotope stage (MIS) 4 (Bartz et al., 2015). However, ephemeral stream deposits are challenging geo-archives for reconstructing landscape changes, since these fluvial systems are highly discontinuous (Bull, 1997). Indeed, it is difficult to distinguish between phases of morphodynamic activity, including both fluvial downcutting and aggradation (e.g. Patton and Schumm, 1981), and morphodynamic stability, mostly indicated by pedogenesis (e.g. Fedoroff and Courty, 2013). This is mostly because climatic and anthropogenic influences as well as autogenous changes may cause spatially variable incision or filling episodes within these fluvial systems (Bull, 1997; Faust et al., 2004; Wolf et al., 2014).

* Corresponding authors.
E-mail addresses: m.bartz@uni-koeln.de (M. Bartz), h.brueckner@uni-koeln.de (H. Brückner).

http://dx.doi.org/10.1016/j.catena.2016.12.007
0341-8162/

Detailed sedimentological and geochemical analyses may help to differentiate phases of variable morphodynamics. Fluvial sediments of perennial river systems, such as the Medjerda River in Tunisia, contain clear features of pedogenesis as indicated by thin section studies (Faust et al., 2004), and intercalated layers deposited by severe flood events inferred from geochemical sediment composition (Zielhofer et al., 2004). In Morocco, Holocene terraces of the Kert River (Barathon et al., 2000; El Amrani et al., 2008) show features of different soil forming phases determined from pedological and sedimentological criteria (Zielhofer et al., 2008). Similar patterns have been observed in deposits of the Moulouya River (Ibouhouten et al., 2010; Zielhofer et al., 2010). Although catchments of ephemeral stream systems are usually much smaller, similar studies can be undertaken. Grain-size analyses of sediments from Wadi Sabra (Jordan) provide evidence of fluvial and fluvio-aeolian sedimentation during MIS 3 and MIS 2, whilst periods of soil formation could be identified by analyses of carbonates and organic matter (Bertrams et al., 2012).

Establishing chronologies for ephemeral stream sediments is likewise challenging. Gastropod shells found in our ephemeral stream profiles could be theoretically sampled for radiocarbon dating, but this material is prone to reworking issues in ephemeral fluvial systems (Rixhon et al., in press). Whilst optically stimulated luminescence (OSL) dating has been successfully applied in such settings (e.g. Bartz et al., 2015; Bubenzer et al., 2007; Klasen et al., 2013), the applicability of OSL dating of quartz is usually limited to ~200 ka due to the low saturation level of the quartz fast component (Wintle and Murray, 2006). For older sediments, infrared stimulated luminescence (IRSL) dating of feldspars may represent a valuable alternative, although IRSL ages may suffer from anomalous fading, leading to a loss of signal over time and possible age underestimation (e.g. Huntley and Lamothe, 2001; Wintle, 1973). In this respect, post-infrared infrared stimulated luminescence dating at an elevated temperature of 290 °C ($pIRIR_{290}$; Thiel et al., 2011) offers feldspar signals which are less affected or unaffected by anomalous fading (Thomsen et al., 2008).

This study thus aims at (i) identifying pedogenetic processes and flooding activity in Wadi Selloum's ephemeral stream deposits as indicators for morphodynamic stability and activity, respectively, using micromorphological, sedimentological, geochemical and mineralogical proxies; (ii) establishing a chronology for the depositional units by a combination of different luminescence dating approaches; and (iii) discussing the Wadi Selloum record in the Late Quaternary palaeoenvironmental context of the Western Mediterranean region and possible correlations of the inferred environmental changes with the phases of occupation in the Ifri n'Ammar rock shelter.

2. Study area

2.1. Climatic and geomorphological setting

The ~290 km^2 wide catchment of the Wadi Selloum, a western tributary of the lower Moulouya river, drains the northernmost prolongation of the Middle Atlas Mountains in NE Morocco (Benjelloun et al., 1971) (Fig. 1a, b). The present climate is semi-arid with annual precipitation ranging between 200 and 600 mm (Snoussi et al., 2002). Most of the rainfall is concentrated during episodic and high-intensity events (Snoussi et al., 2002). The precipitation pattern is reflected by the hydrological regime, dominated by episodic flash floods with rapid flow velocity and high sediment discharge (Abdalla et al., 2014). Rain-fed agriculture and extensive grazing of sheep and goats are common, thus causing recent human-induced soil erosion.

The studied area of the Wadi Selloum encompasses ~20 km^2 of the upper catchment (Fig. 1b, c), exclusively composed of Mesozoic limestone and dolomite (Benjelloun et al., 1971). The ephemeral stream system drains the foothills of the rock shelter of Ifri n'Ammar in a southeastern flow direction, and is fed by two tributaries (Fig. 2a). The ephemeral stream sediments observed in the (sub-)vertical bank profiles generally consist of alternations of coarse-grained (gravel) and fine-grained (silt- and clay-rich) deposits. Whilst the latter is essentially transported as suspension load, the former mostly represents bed load material and is indicative of channel deposits. Given the discontinuity of ephemeral stream systems (Bull, 1997), we observed spatial heterogeneity in the wadi banks. The width of the valley floor is highly variable: it amounts to only ~150 m between the rock shelter and Rock Selloum (Fig. 2a), but rapidly increases downstream, where channel widening is also observed. Several rock fall events occurred along the limestone cliff of Rock Selloum; the deposits of the two largest of them (rf I and rf II) extend to the valley floor directly upstream of Ifri n'Ammar (Fig. 2a). Geomorphological analysis of Quaternary terrace systems of the lowermost Moulouya reach along with a morphometric analysis of the whole Moulouya catchment, including a focus on the Wadi Selloum catchment, highlights a long-term disequilibrium of both the main trunk and the tributary (Barcos et al., 2014; Rixhon et al., 2017). This might be reflected by two 3–4 m-high knickpoints (kp I and kp II; Fig. 2b) disrupting the present-day ephemeral stream

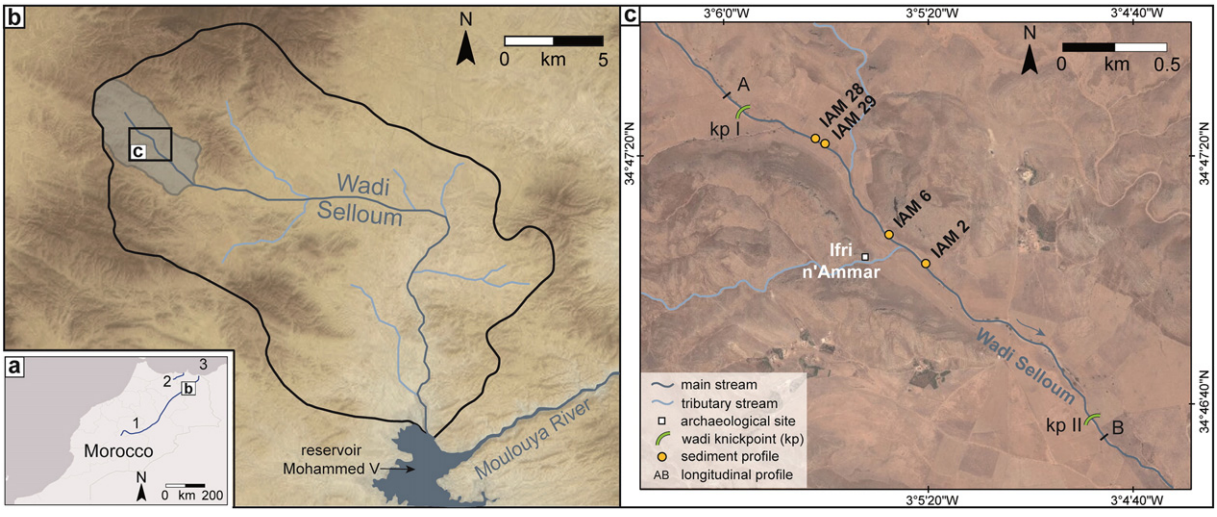

Fig. 1. a: The study area in NE Morocco; 1 – Moulouya River, 2 – Kert River, 3 – Alboran Sea. b: Catchment area of the Wadi Selloum (~290 km^2), a tributary of the lower Moulouya river (based on ASTER Global DEM; USGS, 2015); the studied upper catchment is indicated in grey. c: The upper catchment of the Wadi Selloum in the direct vicinity of the rock shelter Ifri n'Ammar (based on Esri, 2014), presenting the locations of the profiles (IAM 2, IAM 6, IAM 28 and IAM 29) and the knickpoints (kp I and kp II). The bed topography was measured between A and B by DGPS.

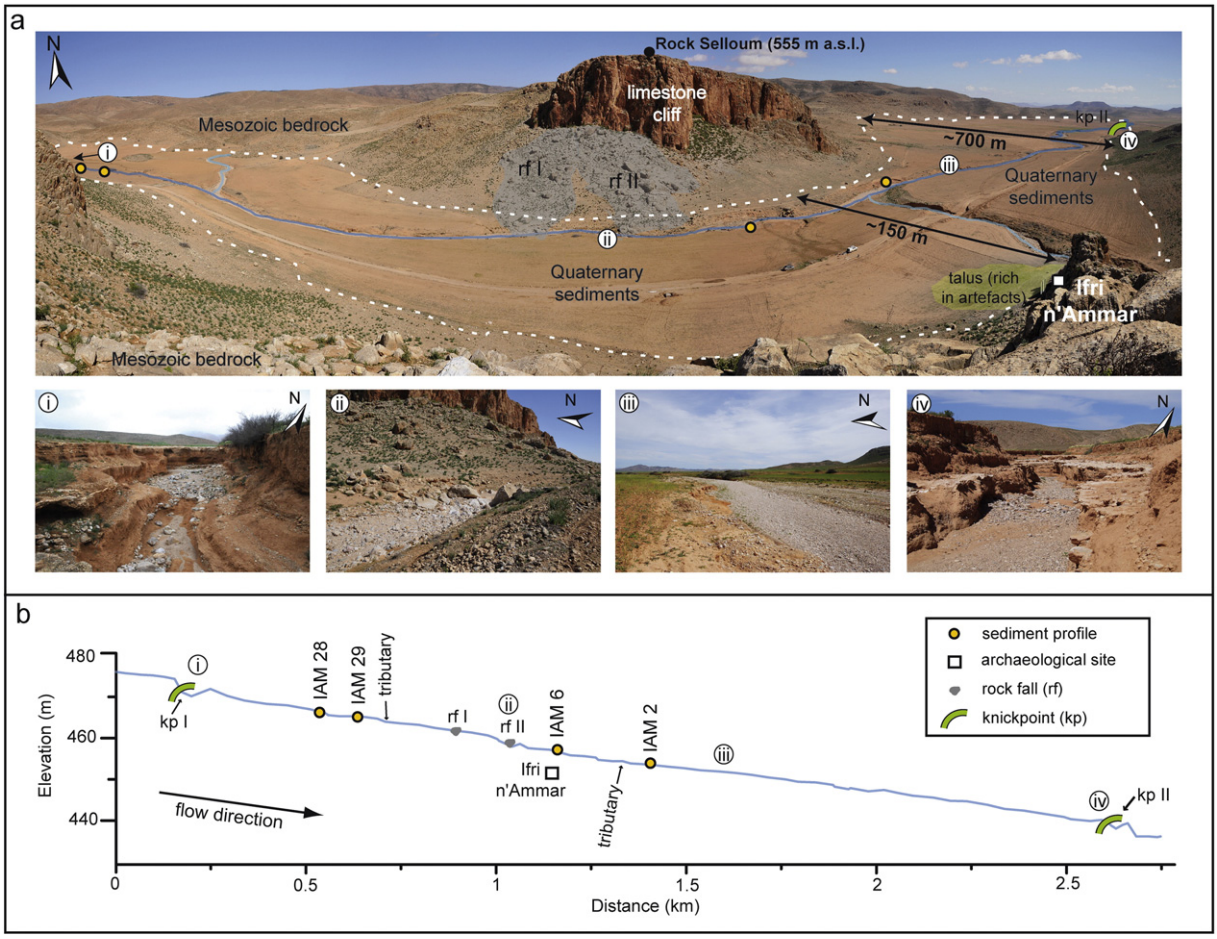

Fig. 2. a: Overview of the Wadi Selloum valley in the vicinity of Ifri n'Ammar; the main geomorphological features are indicated. i – An alternation of coarse-grained gravel and fine-grained overbank deposits at the location of knickpoint (kp) I. The top of kp I is characterised by a dm-thick calcrete. ii – Rock fall (rf) deposits in the main trunk of Wadi Selloum. iii – Downstream of Ifri n'Ammar, the valley bottom of Wadi Selloum widens to ~700 m due to an increase in the accommodation space. iv – Knickpoint (kp) II is characterised by ~2 m-thick profiles with calcretes at the base of the modern stream bed. b: Longitudinal profile of the studied Wadi Selloum section with locations of the photographs i-iv, the investigated profiles, the two knickpoints (kp I and kp II), the two rock falls (rf I an rf II) and the rock shelter of Ifri n'Ammar. The bed topography was measured by DGPS.

channel, although their locations seem closely related to decimetre-thick calcrete crusts within the episodically active stream bed (Fig. 2a).

2.2. Archaeological background

The archaeological layers of the Ifri n'Ammar rock shelter reveal discontinuous phases of AMH settlements during the last ~170 ka. The lower part shows a Middle Palaeolithic sequence (Mikdad et al., 2004; Nami and Moser, 2010), which is dated to time spans between 171 ± 12 ka and 145 ± 9 ka, as well as between 130 ± 8 ka and 83 ± 6 ka (thermoluminescence, TL, ages of heated flint; Richter et al., 2010). The uppermost part of the Middle Palaeolithic sequence has been ^{14}C-dated to a time span between 51.5 ± 1.3 ka BP and 38.9 ± 2.0 ka BP (Linstädter et al., 2012; Mikdad et al., 2002; Moser, 2003). The upper part of the archaeological sequence covers the Upper Palaeolithic related to the Iberomaurusian culture, which is ^{14}C-dated between 13.9 ± 0.08 ka BP (16.8–16.5 ka cal BP) and 10.0 ± 0.08 ka BP (11.7 ± 0.4 ka cal BP) (Linstädter et al., 2012; Moser, 2003).

3. Materials and methods

3.1. Fieldwork and sampling strategy

The current stream bed topography of the main trunk (Fig. 2b) was measured by differential GPS (Topcon DGPS). Ephemeral stream deposits were investigated and documented (FAO, 2006) in four different profiles; the latter are located downstream of (IAM 2), next to (IAM 6) and upstream of (IAM 28 and IAM 29) the archaeological site (Fig. 1c). Within the current stream bed the contact with the carbonate bedrock was not reached in any of the profiles.

From profile IAM 2 (Fig. 3), five luminescence samples were collected at depths of 0.90 (C-L3830), 1.90 (C-L3388), 2.85 (C-L3385), 3.85 (C-L3383) and 4.80 (C-L3389) m below surface (b.s.). Eight micromorphological samples (thin section, TS) were taken at depths of 1.97, 2.32, 2.52, 2.92, 3.22, 3.57, 3.92 and 4.22 m b.s. (TS 2.1–2.8). The profile IAM 2 was sampled in 10 cm intervals down to 4.80 m b.s. Two luminescence samples from profile IAM 6 (Fig. 4), previously dated by OSL (C-L3393 and C-L3395; Bartz et al., 2015), were measured with the pIRIR$_{290}$ dating technique for an inter-method comparison. In addition, two samples for micromorphological studies were taken at 1.05 and 4.50 m b.s. (TS 6.1–6.2). The profile IAM 6 was also sampled in 10 cm intervals down to 4.90 m b.s., except between 2.90 and 4.20 m b.s. where a strongly cemented layer hampered any sampling. From IAM 29 (Fig. 5), two luminescence samples were collected at depths of 0.90 and 1.97 m b.s. (C-L3828 and C-L3829), and samples for micromorphological analyses at 1.50 and 1.97 m b.s. (TS 29.1–29.2). Sediments from the IAM 29 profile were also sampled at 10 cm intervals from the surface to 2.50 m b.s.; we assume that this profile is analogous to the IAM 28 profile (Fig. 5). Four additional samples for micromorphological analyses

were collected in the upper part of the IAM 28 profile (Fig. 6), at depths of 0.40, 0.70, 1.05 and 1.60 m b.s. (TS 28.1–28.4).

3.2. Sedimentological, geochemical and micromorphological analyses

Sediment samples were air-dried and sieved to separate the matrix fraction <2 mm for further analyses. The grain-size distribution was measured three times in 116 classes with a laser particle sizer (Beckman Coulter LS13320) after removal of organic matter with H_2O_2 (10%). After pre-treatment the samples were dispersed overnight within an overhead shaker using 2 ml 0.05 M sodium pyrophosphate ($Na_4O_7P_2$) to avoid coagulation. The GRADISTAT software version 4.0 (Blott and Pye, 2001) was applied for calculation of grain-size parameters after Folk and Ward (1957). The loss on ignition (LOI) was determined by oven-drying (Carbolite ELF 11/14) the samples at 105 °C for 12 h and by ignition in an annealing furnace at 550 °C for 4 h (LOI_{550}; Heiri et al., 2001). The LOI_{550} was used as an indicator for pedogenic accumulation of organic matter, although its accuracy is limited due to possible dehydration of clay or metal oxides, loss of volatile salts or loss of inorganic carbon in minerals (Heiri et al., 2001; Mook and Hoskin, 1982; Sutherland, 1998). Analysis of the mineralogical phases was performed by X-ray diffraction (XRD, Bruker D8-Advance diffractometer with CuKα radiations) on powdered bulk sediment (Moore and Reynolds, 1997). The relative abundance of minerals (including carbonates) was estimated from the height of the main peak with the DIFFRACplus EVA software (Boski et al., 1998; Cook et al., 1975). Thin section preparation followed the procedure of Beckmann (1997). The observations were performed with a polarising transmitted-light microscope and description followed the guidelines of Stoops (2003). The colours of dried sediments and soil material were determined with the Munsell Soil Color Chart. Soil identification followed the "World Reference Base for Soil Resources" (IUSS Working Group WRB, 2014).

3.3. Application of luminescence dating techniques to ephemeral stream deposits

Sample preparation for dose measurements included treatment with H_2O_2 (10%), HCl (10%) and sodium oxalate to remove carbonates, organics and clay remains. Whilst density separation with sodium polytungstate was used to isolate coarse-grained (100–150 μm) quartz (ρ_1 = 2.62–2.68 g cm^{-3}) and feldspars (ρ_2 ≤2.58 g cm^{-3}), the polymineral fine-grained fraction (4–11 μm) was extracted using a centrifuge. The quartz minerals were etched with HF (40%) for 40 min plus a final HCl (10%) wash.

All measurements were carried out in the Cologne Luminescence Laboratory (CLL) on automated Risø TL/OSL DA 20 readers equipped with $^{90}Sr/^{90}Y$ beta sources for irradiation, delivering dose rates of ~0.08 Gy s^{-1}. Quartz multiple-grain signal emissions (1 mm and 2 mm aliquots) were detected using blue light emitting diodes (470 ± 20 nm) and a Hoya U 340 glass filter (7.5 mm), whereas quartz single grains were stimulated for 2 s with a green Nd:YVO_4 diode-pumped laser (532 nm) (Bøtter-Jensen et al., 2000). Equivalent dose (D_e) determination followed the single-aliquot regenerative-dose (SAR) protocol of Murray and Wintle (2000, 2003), using the initial part of the decay curve (0–0.8 s) after subtraction of a late background (36–40 s) for quartz multiple-grain aliquots. For single-grain measurements, the OSL signal was derived from the first 0.054 s of stimulation minus a background of the last 0.4 s. A preheat-plateau test with increasing temperatures between 180 and 280 °C (held for 10 s), in combination with a cut heat 20 °C below the preheat temperature, was performed for sample C-L3828 to determine the appropriate thermal pre-treatment (7 multiple-grain aliquots per temperature step). Dose recovery tests (given dose = 80 Gy), in combination with different preheat temperatures, were conducted using 100 s blue-LED stimulation at room temperature (~25 °C) for signal resetting. To investigate the OSL signal components, fitting of continuous wave (CW)-OSL curves was applied. CW-OSL measurements were carried out on three aliquots of sample C-L3828 and fitted using the software package R-Luminescence (Kreutzer et al., 2012).

IR stimulation (880 ± 80 nm) and signal detection through an interference filter (410 nm) were used for measuring the coarse-grained feldspar samples and the fine-grained polymineral sample. The first 2.4 s of stimulation minus a background of the last 40 s were used. The pIRIR signal was measured at 290 °C ($pIRIR_{290}$; Thiel et al., 2011) for 200 s after a preheat of 320 °C (hold for 60 s). At the end of each cycle, a 325 °C IR bleaching was used. The prior IR stimulation temperature was chosen by performing prior IR stimulation temperature tests on three coarse-grained feldspar samples (C-L3395, C-L3829, C-L3830) and on the fine-grained polymineral sample C-L3389 to investigate the dependency of D_e on prior IR stimulation (Buylaert et al., 2012). Although results of Thiel et al. (2011) and Buylaert et al. (2012) suggest that the $pIRIR_{290}$ seems to be unaffected by anomalous fading, sample C-L3395 was checked for anomalous fading using the procedure of Auclair et al. (2003). A bleaching test with optical treatment in the solar simulator (Hönle SOL2) between 0.5 and 24 h was carried out for sample C-L3389 to test the bleaching characteristics of the $pIRIR_{290}$-protocol. Furthermore, dose recovery (given doses commensurate with D_e of each sample) and residuals after 24 h signal resetting in the solar simulator were determined for all samples.

The measured aliquots had to fulfil the following SAR rejection criteria for both quartz and $pIRIR_{290}$ samples: (i) test dose error ≤10%; (ii) recuperation <5% of the sensitivity-corrected natural signal; (iii) recycling ratio between 0.9 and 1.1 (for single grains between 0.85 and 1.15); (iv) $D_e < 2 * D_0$; and (v) IR depletion ratio ≤10% (Duller, 2003). The central age model (CAM; Galbraith et al., 1999) was used for D_e calculation.

High-resolution γ-spectrometry using a high-purity germanium detector was carried out for dose rate determination. DRAC v1.1 (Durcan et al., 2015) was applied for dose rate and age calculation using the conversion factors of Guérin et al. (2011), and alpha and beta attenuation factors of Bell (1980) and Guérin et al. (2012); the latter was specifically chosen for either quartz or feldspar grains. The contribution of cosmic dose rates was assessed following the approach of Prescott and Hutton (1994). To account for attenuation of ionising radiation by pore water, field water contents (mass of water relative to the dried sample) of 4–20% were considered with an uncertainty of ~30%. For coarse-grained feldspar, an α-efficiency of 0.11 ± 0.03 (Balescu and Lamothe, 1993) was used, whilst an α-efficiency of 0.07 ± 0.02 (Preusser et al., 2005) was assumed for polymineral fine grains. An internal potassium content of 12.5 ± 0.5% (Huntley and Baril, 1997) was assumed for feldspars.

4. Results

4.1. Profile descriptions

In the following, the investigated profiles are described from their positions downstream to upstream of the rock shelter of Ifri n'Ammar. Depths of all units or their boundaries are given below surface (b.s.).

4.1.1. Profile IAM 2

The bipartite, ~5 m-high profile IAM 2 (Fig. 3) is located ~230 m to the east of Ifri n'Ammar (Fig. 1c). Reddish yellow (7.5YR 6/6) silts form unit 1 (5.00–4.00 m). They include sparse charcoal remains, terrestrial gastropods (e.g. *Otala* cf. *lactea*) and carbonate precipitations. Reddish yellow (7.5YR 6/6) sandy silts, embedding

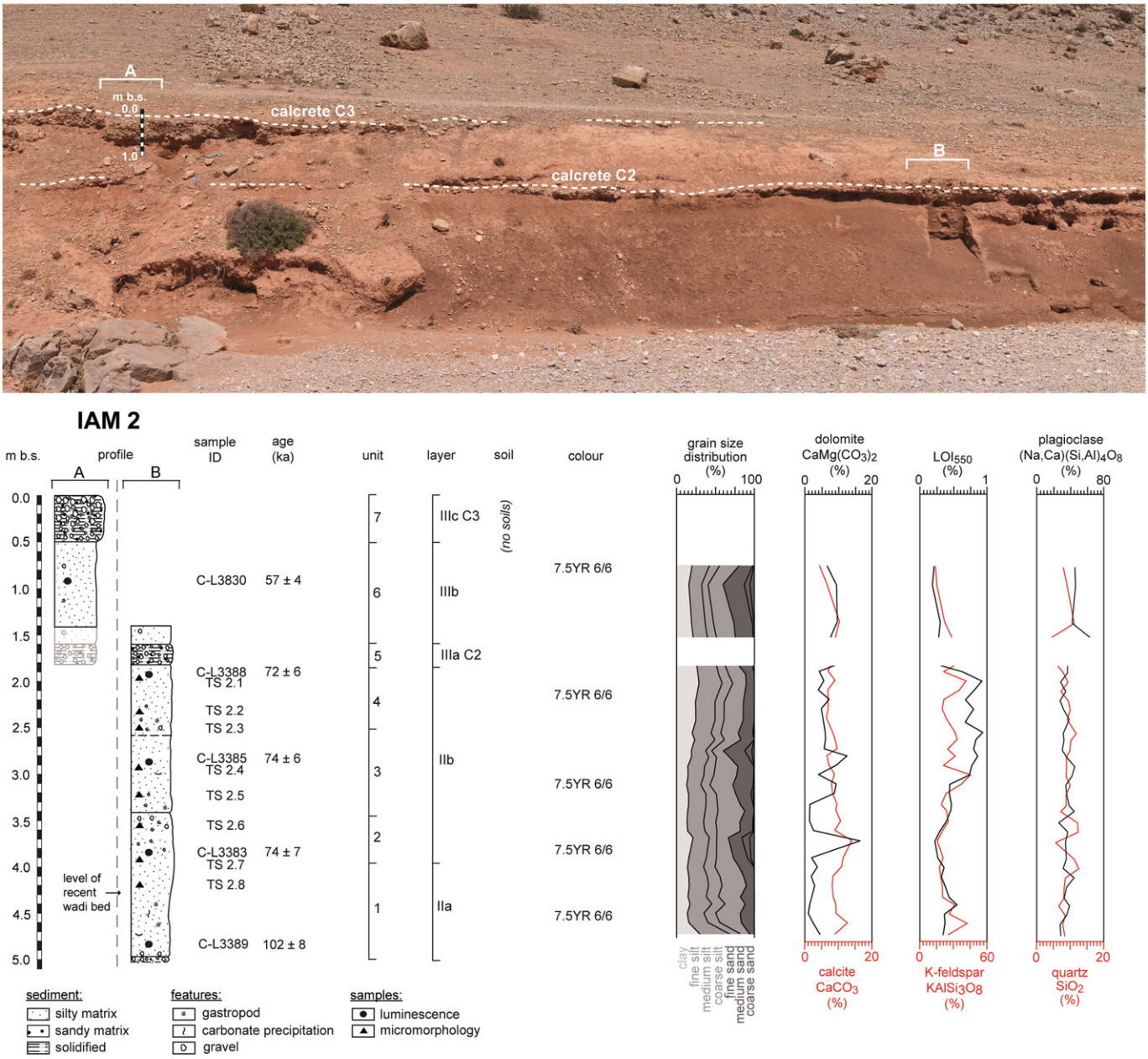

Fig. 3. Stratigraphical record of profile IAM 2 including sedimentological and geochemical results. Samples for luminescence dating and micromorphology are indicated with depths, ages and sample IDs. Sediment units of each profile as well as layers for profile correlation in the catchment are presented together with pedogenic features. The two calcretes C2 and C3 (white dashed lines) can be used to correlate parts A and B of the bipartite profile IAM 2.

sparse, subangular, up to 2 cm-large gravel, form unit 2 (4.00–3.40 m). Reddish yellow (7.5YR 6/6) sediments with a coarsening-upward tendency, from fine sandy silts to silty fine sands, form unit 3 (3.40–2.50 m), including a few specimens of *Otala* cf. *lactea* and charcoal remains. The overlying stratum at 2.50–1.80 m (unit 4) shows a silty matrix with a reddish yellow (7.5YR 6/6) sediment colour. The base of unit 5 is marked by an erosional unconformity at 1.80 m. This unit (1.80–1.60 m) is formed by solidified gravels of up to 10 cm in size (C2). Marked by a sharp basal boundary, the homogeneous unit 6 (1.60–0.50 m) is formed by reddish yellow (7.5YR 6/6) sandy silts, embedding sparse, subangular, up to 3 cm-large gravel. The top 0.60 m-thick solidified layer (unit 7; C3) is composed of up to ~20 cm-large gravel.

4.1.2. Profile IAM 6

The ~4.90 m-high profile IAM 6 (Fig. 4) is located ~150 m to the northeast of Ifri n'Ammar (Fig. 1c). We refer to the stratigraphic description of Bartz et al. (2015) for this profile. Reddish yellow (7.5YR 6/6) sandy silt form the lowermost unit 1 (4.90–4.10 m). The base of the composite unit 2 is marked by an erosional unconformity at 4.10 m. Gravels in a sandy matrix are cemented in the lower part of unit 2 (4.10–3.65 m), forming a calcrete layer (C2); they are less solidified in the middle part (3.65–3.00 m). The upper part of unit 2 (3.00–2.30 m) is formed by reddish yellow (7.5YR 6/6) silty sands. The overlying unit 3 (2.30–2.10 m) is characterised by gravel in a sandy matrix. The uppermost unit 4 of the profile (2.10–0 m) is characterised by a fining-upward

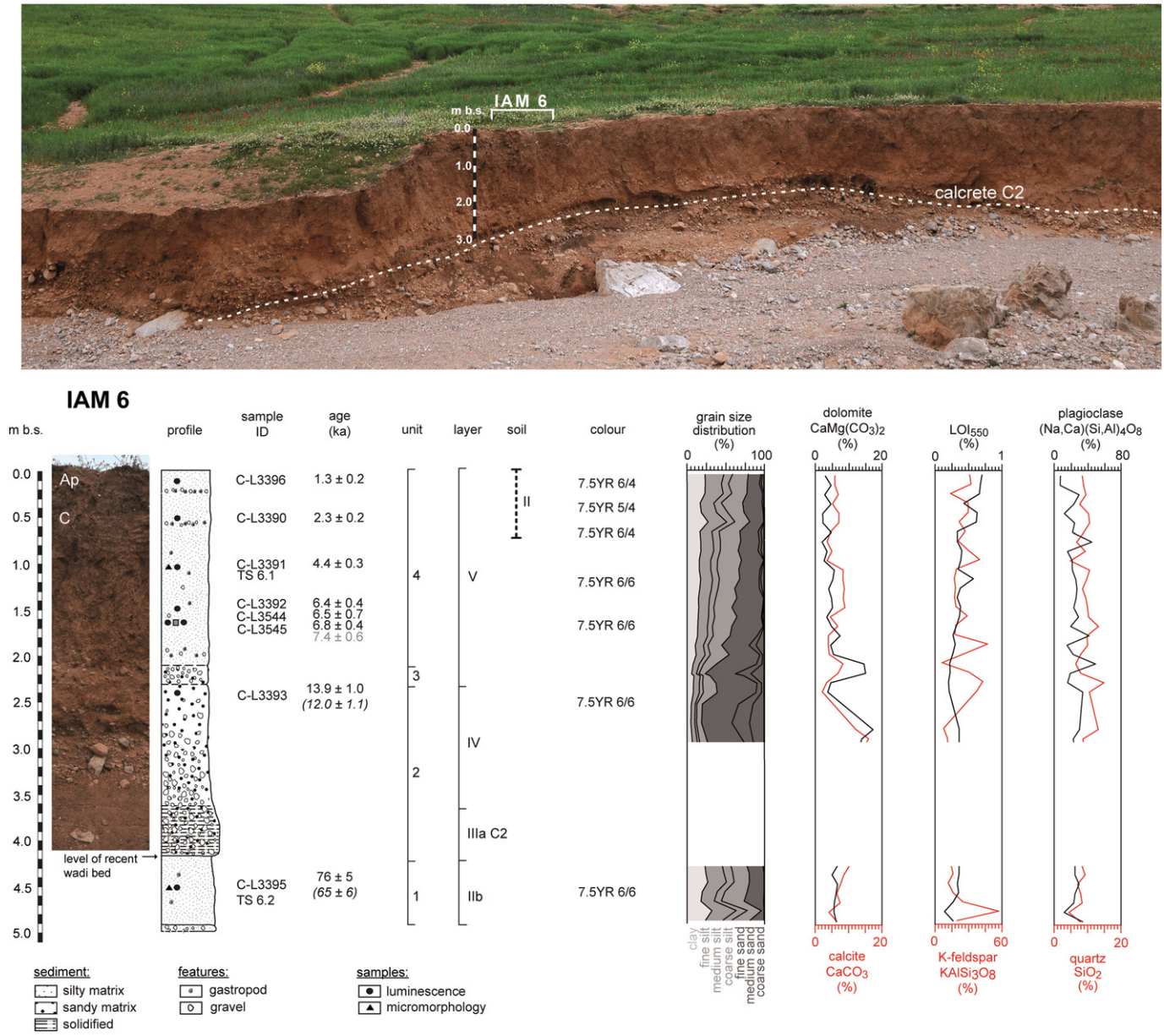

Fig. 4. Stratigraphical record of profile IAM 6 (modified from Bartz et al., 2015) including sedimentological and geochemical results. Samples for luminescence dating and micromorphology are indicated with depths, ages ($pIRIR_{290}$ ages in brackets for an inter-method comparison) and sample IDs. Sediment units of each profile as well as layers for profile correlation in the catchment are presented together with pedogenic features. The white dashed line in the upper photograph indicates the top of the calcrete C2.

sequence from silty fine sands to fine sandy silts. It is interspersed by layers of well-preserved terrestrial gastropods (e.g. *Otala* cf. *lactea*, *Rumina decollata*) and pieces of charcoal at 0.60 and 0.20 m. A change in the sediment colour to light brown (7.5YR 6/4) is observed from 0.40 m up to the top.

4.1.3. Profile IAM 29

The ~3.20 m-high profile IAM 29 (Fig. 5) is located ~600 m to the northwest of Ifri n'Ammar (Fig. 1c). The 0.60 m-thick basal unit 1 (3.20–2.60 m) is composed of up to 10 cm-large, subangular carbonate gravel and stones (C1), cemented by a calcareous sandy matrix. The overlying unit 2 (2.60–1.70 m) is dominated by reddish yellow (7.5YR 6/6) sandy silts, intercalated by a gravel-dominated layer (2.35–2.20 m) composed of 5 cm-large subangular components. The unit 3 (1.70–1.30 m) is characterised by reddish (7.5YR 7/4), clay-rich silts, with up to 2 cm-large carbonate nodules. The overlying unit 4 (1.30–1.15 m) is composed of up to 10 cm-large subangular gravel, embedded in clay-rich silts. The uppermost unit 5 (1.15–0 m) is a coarsening-upward sequence from clay-rich silts to fine sandy silts. The sediment colour changed from reddish yellow (7.5YR 7/6) to yellowish brown (10YR 5/4). The uppermost layer of the profile (0.60–0 m) includes organic material (e.g. roots), terrestrial gastropods (e.g. *Otala* cf. *lactea*) as well as carbonate and dolomite fragments.

4.1.4. Profile IAM 28

The ~3.20 m-high profile IAM 28 (Fig. 6) is situated ~40 m upstream of profile IAM 29 (Fig. 1c). Since both profiles present similar sediment characteristics, the unit classification of IAM 29 is adopted for this profile. Basal gravels (C1) form unit 1 (3.20–2.60 m). Light

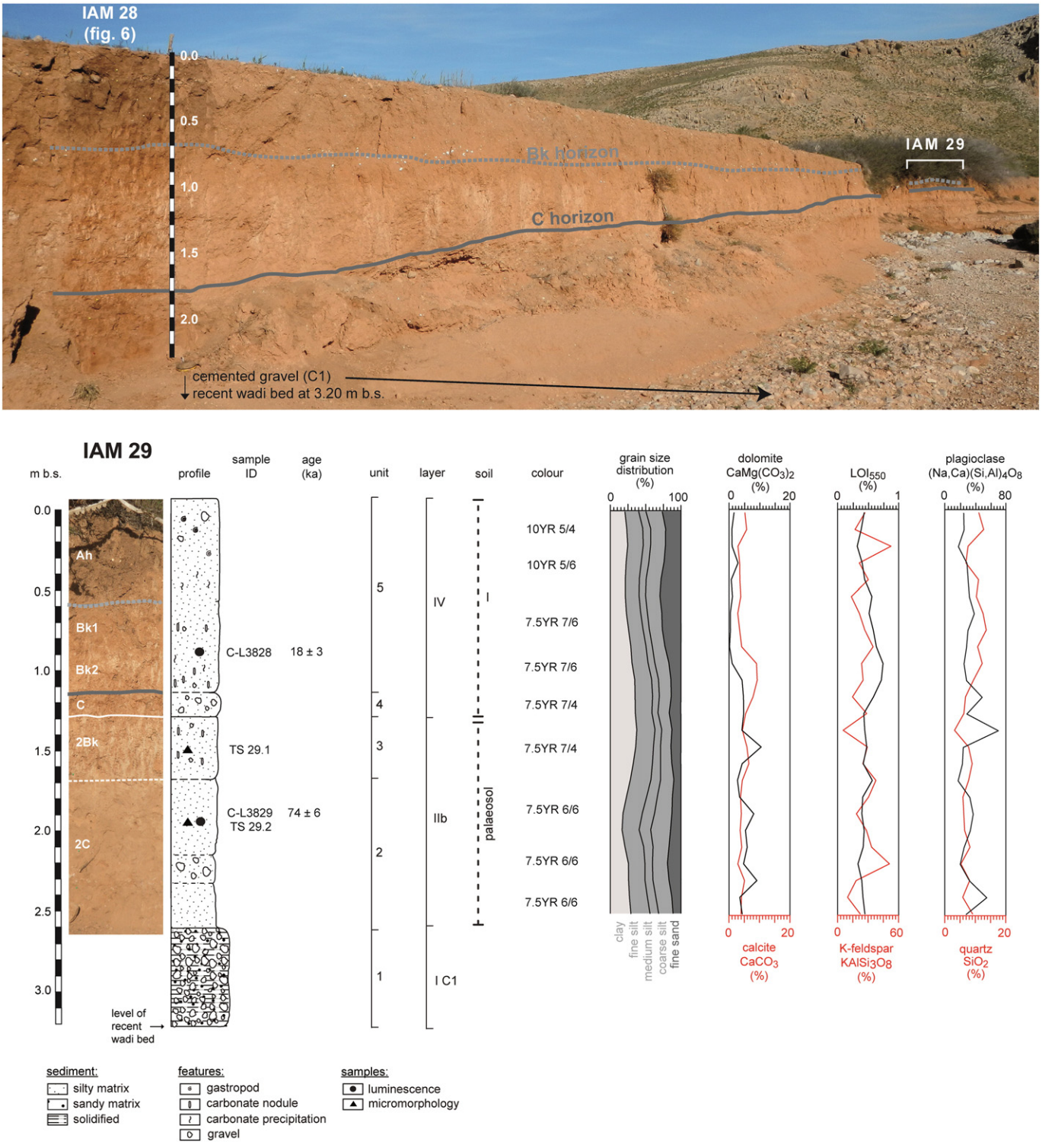

Fig. 5. Upper part: profiles IAM 28 and IAM 29 viewed from the ephemeral stream bed. They can be correlated by the Bk horizon (light grey dashed line) and the C horizon (dark grey solid line). Lower part: stratigraphical record of profile IAM 29 including sedimentological and geochemical results. Samples for luminescence dating and micromorphology are indicated with depths, ages and sample IDs. Sediment units of each profile as well as layers for profile correlation in the catchment are presented together with pedogenic features. See Fig. 6 for the detailed description of profile IAM 28.

brownish (7.5YR 6/4) silts compose unit 2 (2.60–2.15 m). The overlying yellowish/reddish (7.5YR 7/4 to 7/6), clayey/silty unit 3 (2.15–1.95 m) is characterised by well-developed subangular blocky peds and up to 2 cm-large carbonate nodules. Unit 4 (1.95–1.80 m) is composed of subangular gravel (~10 cm in size). The uppermost unit 5 (1.80–0 m) shows colour changes from reddish yellow (7.5YR 7/6) to yellowish brown (10YR 5/4). A compact clay-rich silt was observed from 1.80 to 0.60 m; it also exhibits carbonate

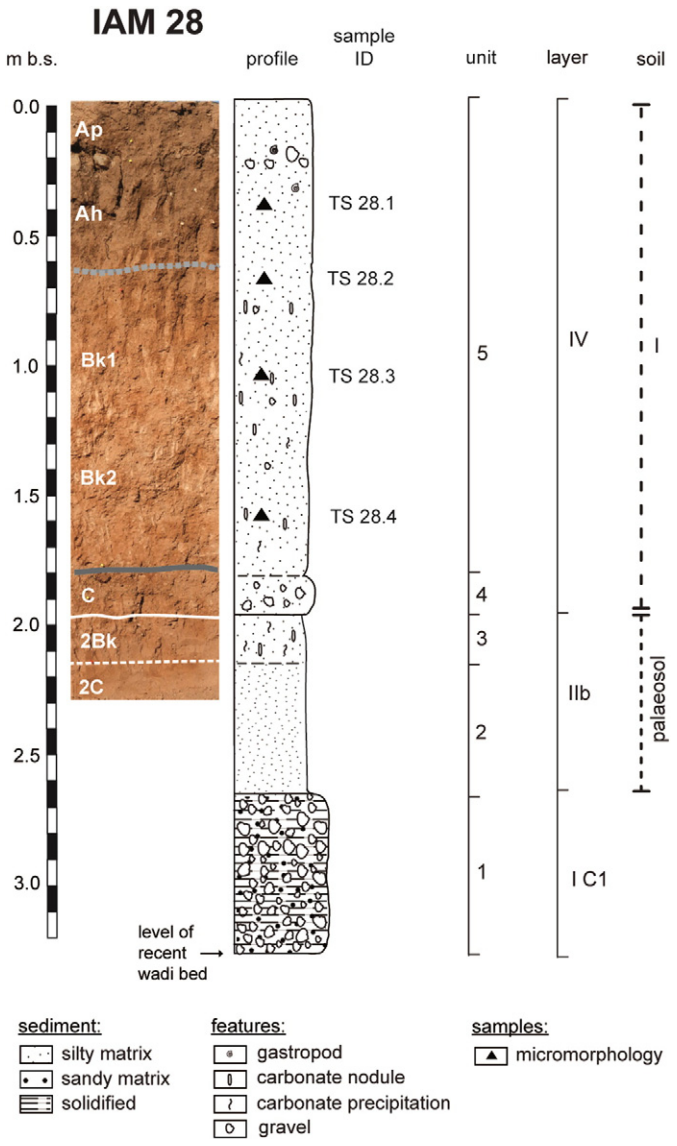

Fig. 6. Stratigraphical record of profile IAM 28. Micromorphological samples are indicated with depths and sample IDs. Sediment units of each profile as well as layers for profile correlation in the catchment are presented together with pedogenic features. Profile IAM 28 is correlated with profile IAM 29 (see Fig. 5).

precipitations and up to 1 cm-large nodules. The latter only occur up to 0.95 m, whereas carbonate precipitation was observed up to ~0.40 m. Furthermore, the sediment structure is characterised by slightly developed blocky peds from 0.95 to 0.60 m. The uppermost layer of the profile (0.60–0 m) includes occasional roots, subangular gravel (~3 cm in diameter) and terrestrial gastropods (e.g. *Otala* cf. *lactea*).

4.2. Sediment properties and soil micromorphology

The results of micromorphological analyses are presented in Tables 1 and 2. According to similar characteristics and recurring patterns observed in the 16 thin sections (TS), they may be classified into three distinct groups. Group 1 has characteristic A horizon features, group B relates to B horizons, and group 3 points to sediments weakly altered by pedogenesis (C horizons).

4.2.1. A horizon features

Group 1 encompasses TS 28.1, 28.2 and 6.1 (Fig. 7). The silty and sandy fractions are dominated by angular to subangular quartz, K-feldspar and plagioclase grains (Fig. 7d). The coarser fabric units occur unsorted in a dense matrix, which results in a single (TS 28.1) to double (TS 6.1 and TS 28.2) spaced porphyric c/f-related distribution. Whilst TS 28.1 shows a partly undifferentiated b-fabric, the TS display a calcitic crystallitic b-fabric due to dispersed micrite in the groundmass. Primary carbonates, mostly corresponding to fragments of gastropod shells and carbonate rocks, are only present in small amounts which is in agreement with rather small values of both dolomite and calcite. The TS are characterised by moderately developed pedality and ped separation (Fig. 7a–c). The microstructure is spongy, crumb and granular, which can be related to infillings in burrows and to bioturbated parts of the TS. Less than 1 mm small pieces of charcoal are evident. Most of the crumbs are mammilated excrements. Some circular or ellipsoidal burrows with perfectly smooth walls consisting of compacted fine-grained material are evident. Pedofeatures are rare; only a few Fe and Mn nodules occur in the groundmass. Only TS 28.2 is characterised by low abundance of secondary carbonate coatings along voids in the lower parts of the section (Fig. 7e). Very rarely, dusty clay coatings with poorly oriented clay along mineral grains were observed. The darkening of the topsoil in comparison to the subsoil is related to an enrichment of organic material (Ah horizon), although the organic content of the A horizons are rather low with values of LOI_{550} <1%. An Ap horizon describes the topsoil which is influenced by tillage, but otherwise with similar characteristics as the Ah horizon.

4.2.2. B horizon features

Group 2 encompasses TS 28.3, 28.4 and 29.1 (Fig. 8). The c/f-related distribution is single- (TS 28.4) to double- (TS 28.4 and 29.1) spaced porphyric, dominated by silt- to sand-size quartz and feldspar grains. In these B horizons, precipitation of secondary carbonates is the most prominent feature, however, abundant grains of primary carbonate (shell and rock fragments) are found as well. The richness in calcareous components is reflected in high amounts of calcite and dolomite. In addition, the B horizons are characterised by the development of a subangular-blocky microstructure, which, in the case of TS 28.4 is weakly developed. The aggregation is conspicuous due to the development of well-separated subangular blocky peds (Fig. 8a–c), especially in TS 29.1 where aggregates are separated by planes (Fig. 8c). The degree of pedality is moderate (TS 28.3 and 29.1) to weak (TS 28.4). TS 28.4 shows unaccommodated peds, whilst in TS 28.3 and 29.1 peds are partially accommodated. As voids, mainly planes are visible beside chambers and channels. All TS show a crystallitic b-fabric, due to finely-dispersed calcite grains. Various pedofeatures occur: infillings of secondary carbonate (Fig. 8d, e), calcite coatings (Fig. 8g–i), and Fe and Mn nodules (Fig. 8e). Intercalations are visible in TS 28.4 (Fig. 8f). Oriented clay is only documented in form of thin coatings around quartz and feldspar grains. Calcite depletion pedofeatures were not found. Rarely biogenic pedofeatures are visible in form of mammilated excrements and passage features. The subsoil horizons Bk1 and Bk2, respectively, are characterised by different degrees of carbonate precipitation.

4.2.3. C horizon features

Group 3 encompasses TS 2.1–2.8, 6.2 and 29.2 (Fig. 9). Mineral grains are distinguished by a subangular to angular shape in a single- to double-spaced porphyric c/f-related distribution of the groundmass. Beside quartz, K-feldspar and plagioclase minerals, all TS contain primary carbonates, mainly corresponding to calcite and dolomite grains and shell remains. Charcoal residues rarely occur in the groundmass. Rounded aggregates are randomly formed in the sediment and are composed of finer material than the micromass

Table 1
Micromorphological results of thin section (TS) analyses focusing on structure and groundmass features as well as residues of biogenic origin. The observations were performed with a polarising transmitted light microscope. The descriptions follow the guidelines of Stoops (2003): – = none; (•) = rarely; • = few; •• = moderate; ••• = dominant.

Sample ID	TS group	Soil horizon	Structure								Groundmass			
			Aggregation			Voids					Microstructure	c/f-rel. distr.	b-Fabric	Residues of biologic origin	
			Ped separation	Degree of developed pedality	Accommodation	Packing voids	Chambers	Channels	Planes	Vughs				Charcoal	Gastropod shell
TS 2.1	3	C	Weakly separated	Weakly developed	Unaccommodated	•	••	••	•	••	Chamber-channel, locally subangular blocky or granular	Double-spaced porphyric	Crystallitic	(•)	•
TS 2.2	3	C	–	–	–	•	•••	••	–	••	Chamber and granular	Single-spaced porphyric	Crystallitic	–	•
TS 2.3	3	C	–	–	–	•	••	••	–	•	Chamber-channel and granular	Single-spaced porphyric	Crystallitic	(•)	(•)
TS 2.4	3	C	–	–	–	•	••	••	•	••	Chamber-channel and granular	Single-spaced porphyric	Crystallitic	(•)	(•)
TS 2.5	3	C	–	–	–	•	••	•••	–	•	Chamber-channel and granular	Double-spaced porphyric	Crystallitic	(•)	(•)
TS 2.6	3	C	–	–	–	•	••	••	–	•	Chamber-channel and granular	Single-spaced porphyric	Crystallitic	–	•
TS 2.7	3	C	–	–	–	•	••	••	–	••	Chamber-channel and granular	Double-spaced porphyric	Crystallitic	(•)	(•)
TS 2.8	3	C	Weakly separated	Weakly developed	Unaccommodated	•	•••	•••	–	••	Chamber-channel, locally subangular blocky and granular	Double-spaced porphyric	Crystallitic	(•)	•
TS 6.1	1	A	Moderately separated	Moderately developed	Unaccommodated	••	••	••	–	••	Spongy, subangular blocky and granular	Double-spaced porphyric	Crystallitic	(•)	•
TS 6.2	3	C	–	–	–	•	••	••	•	••	Chamber-channel, locally granular	Single-spaced porphyric	Crystallitic	–	(•)
TS 28.1	1	Ap	Moderately separated	Moderately developed	Unaccommodated	••	•••	•••	–	•	Spongy, chamber-channel and granular	Single-spaced porphyric	Crystallitic, partly undifferentiated	(•)	•
TS 28.2	1	A/B	Moderately separated	Moderately developed	Unaccommodated	••	••	••	•	•	Chamber-channel, subangular blocky and granular	Double-spaced porphyric	Crystallitic	(•)	•
TS 28.3	2	Bk1	Moderately separated	Moderately developed	Partially accommodated	–	•	•	•••	•	Subangular blocky, partly massive	Double-spaced porphyric	Crystallitic	–	(•)
TS 28.4	2	Bk2	Weakly separated	Weakly developed	Unaccommodated	•	••	••	••	•	Massive, partly subangular blocky or granular	Single-spaced porphyric	Crystallitic	–	•
TS 29.1	2	2Bk	Moderately separated	Moderately developed	Partially accommodated	••	••	••	•••	••	Subangular blocky, partly massive	Double-spaced porphyric	Crystallitic	–	•
TS 29.2	3	2C	–	–	–	•	•••	•••	•	••	Chamber-channel, partly single-grain	Single-spaced porphyric	Crystallitic	–	(•)

Table 2
Micromorphological results of thin section (TS) analyses focusing on pedofeatures. The observation was performed with a polarising transmitted light microscope. The descriptions follow the guidelines of Stoops (2003): – = none; (•) = rarely; • = few; •• = moderate; ••• = dominant.

Sample ID	TS group	Soil horizon	Calcitic pedofeatures				Fe/Mn pedofeatures		Biogenic pedofeatures			Others
			Hypocoatings	Coatings	Infillings	Nodules	Nodules	Coatings	Mammilated or spherical excrements	Sediment cocoons	Passage features	Intercalations
TS 2.1	3	C	•	•	•	•	••	–	•	(•)	(•)	–
TS 2.2	3	C	–	–	•	–	•	–	•	(•)	•	–
TS 2.3	3	C	–	–	•	–	•	–	(•)	••	(•)	–
TS 2.4	3	C	–	–	–	–	•	–	•	•	(•)	–
TS 2.5	3	C	–	–	–	–	•	–	••	–	(•)	–
TS 2.6	3	C	–	–	–	–	•	–	•	•	(•)	–
TS 2.7	3	C	–	–	–	–	•	•	(•)	(•)	–	–
TS 2.8	3	C	–	–	–	–	•	–	•	–	•	–
TS 6.1	1	A	–	–	–	–	•	–	••	•	(•)	–
TS 6.2	3	C	–	–	–	–	•	–	–	•	(•)	–
TS 28.1	1	Ap	–	–	–	–	•	–	•••	(•)	•	–
TS 28.2	1	A/B	–	(•)	–	–	•	–	•••	•	(•)	–
TS 28.3	2	Bk1	–	•	••	••	••	–	(•)	–	(•)	–
TS 28.4	2	Bk2	–	•	••	••	••	–	–	–	•	•
TS 29.1	2	2Bk	••	•	•••	••	••	–	(•)	–	–	–
TS 29.2	3	2C	•	–	–	–	••	–	••	••	••	–

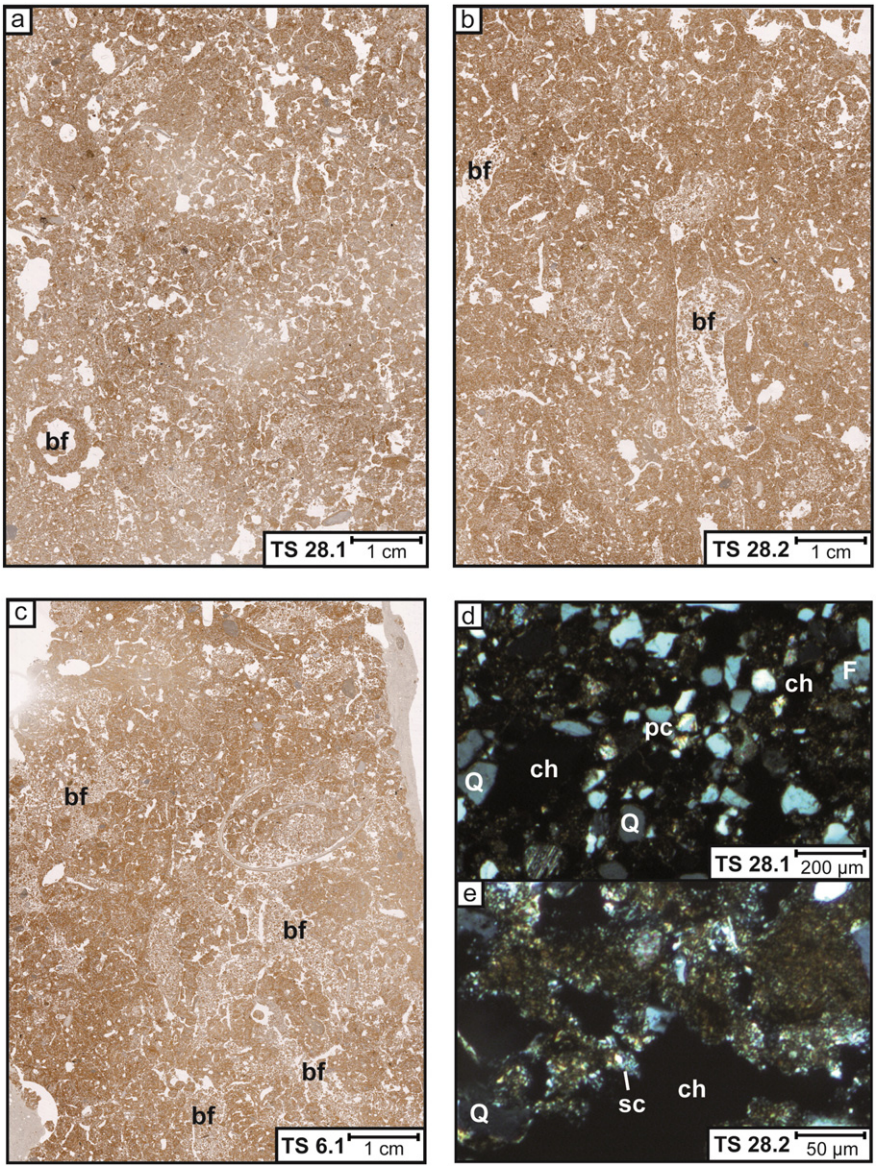

Fig. 7. Thin sections (TS) 28.1, 28.2 and 6.1 associated to TS group 1 (A horizon features). a–c: Flatbed scans characterised by bioturbation features (bf) and the presence of biogenic aggregates. d: Mainly quartz (Q) and feldspar (F) are visible beside rarely distributed primary carbonates (pc, here in form of rock fragments) under crossed-polarised light (XPL). e: Quartz minerals occur unsorted in a dense fine matrix with a crystallitic b-fabric (XPL). Note the slight degree of secondary carbonate (sc) precipitation along voids, e.g. chambers (ch).

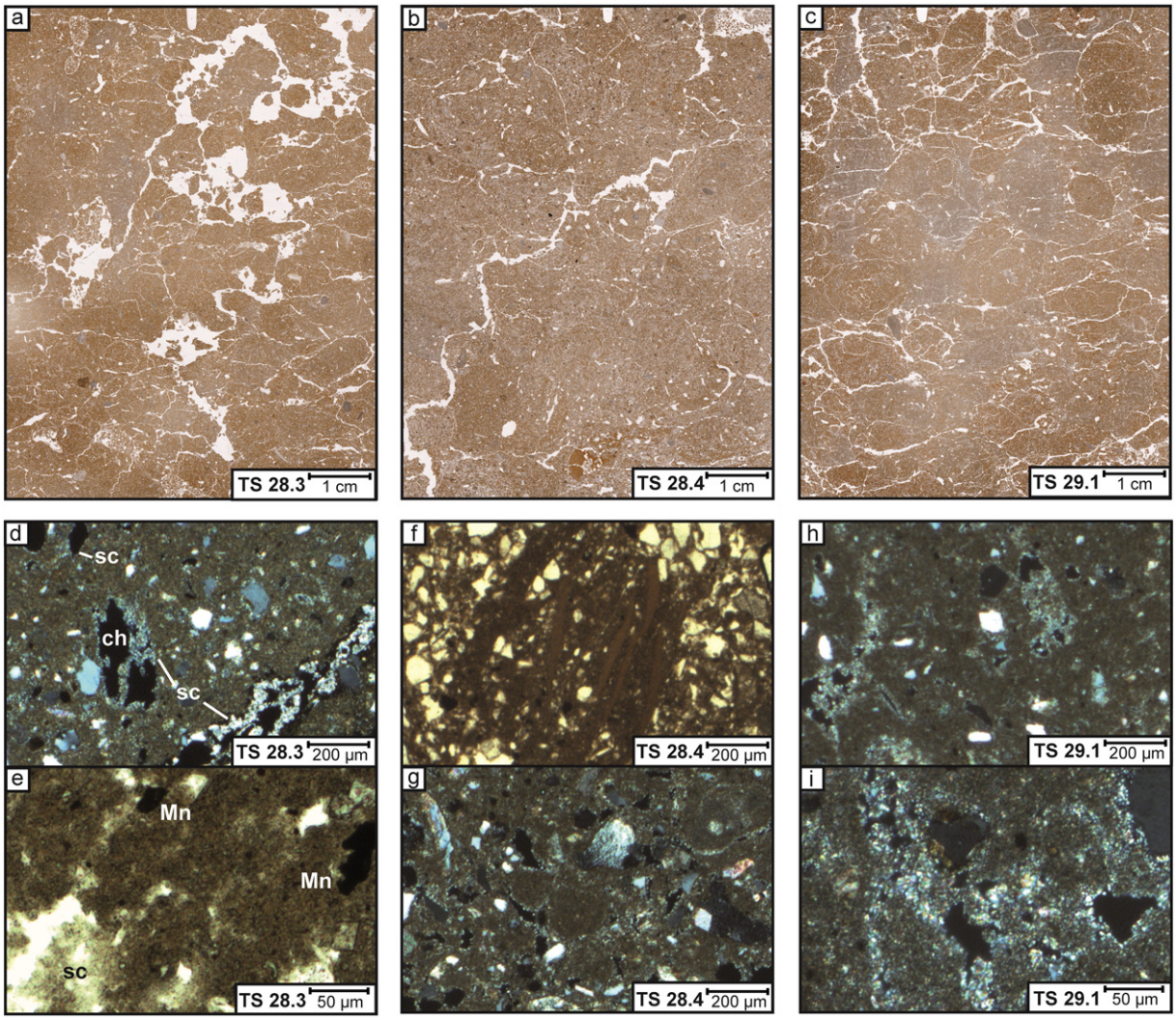

Fig. 8. TS 28.3, 28.4 and 29.1, associated to TS group 2 (B horizon features). a-c: flatbed scans, indicating aggregation in form of subangular blocky peds. d: Secondary carbonate (sc) precipitation in form of infillings and calcite coatings along chambers (ch) in a dense matrix under crossed-polarised light (XPL). e: Secondary carbonate (sc) precipitation in chambers as infillings as well as Mn nodules under plain-polarised light (PPL). f: Intercalation of fine sediment in a coarser matrix characterised by silt- to sand-sized rock fragments (PPL). g, h, i: Precipitation of secondary carbonate along voids (XPL).

(Fig. 9h, i, k, n). The microstructure is a mixture of channel, chamber and granular types. A crystallitic b-fabric is mainly expressed. Accommodation is insignificant and, occasionally, pedality is weakly developed. Voids occur frequently as chambers and channels, partly as vughs and packing voids. Pedofeatures are rare and mainly consist of Fe and Mn nodules. Sparse hypocoatings are found in TS 2.1, 6.2 and 29.2 (Fig. 9g, l, m, o). Precipitation of secondary carbonates is visible in form of infillings to a slight degree in TS 2.1 (Fig. 9f), 2.3 and 2.4. The fluvial nature of the sediment is evident by locally preserved microlayers, showing a fining-upward sequence (Fig. 9j). Biogenic pedofeatures in form of mammilated excrements, sediment cocoons and passage features occur rarely. LOI_{550} values are rather low (<1%).

4.3. Soil identification

Three soils have been identified in the Wadi Selloum deposits: profiles IAM 28 and IAM 29 (Figs. 5, 6) comprise one buried soil in form of a 2Bk-2C sequence (palaeosol) in units 2 and 3, and a second soil characterised by an Ah-Bk1-Bk2-C sequence (soil I) in units 4 and 5. Here, the two Bk horizons provide information about age-related carbonate precipitation. The 2Bk horizon of the palaeosol is characterised by high and intensive precipitation of secondary carbonate and strong pedality (TS group 2, Fig. 8). Soil I belongs to the Calcisol group displaying processes of dissolution of primary carbonates in the A horizons (TS group 1, Fig. 7) and precipitation of secondary carbonates in the B horizons (TS group 2, Fig. 8). As based on the similarity of soil properties with the modern Bk horizon at profiles IAM 28 and IAM 29, the palaeosol may thus represent a subsoil horizon of a former Calcisol. Profile IAM 6 (Fig. 4) reveals pedofeatures characteristic for A horizons (TS group 1, Fig. 7) which are found at ~1 m depth (Fig. 4), reflecting intense bioturbation near a former land surface. Here, a third soil is formed characterised by an Ap-C sequence (soil II) and classified as a weakly developed Fluvisol. Below the A horizon, a clear differentiation in soil horizons is not evident, probably because aggradation of young sediments hampered formation of a Calcisol.

4.4. Geochronological framework

4.4.1. Luminescence properties and D_e determination

Only sample C-L3828 (profile IAM 29) revealed a quartz signal below saturation level. For this sample, a preheat temperature of

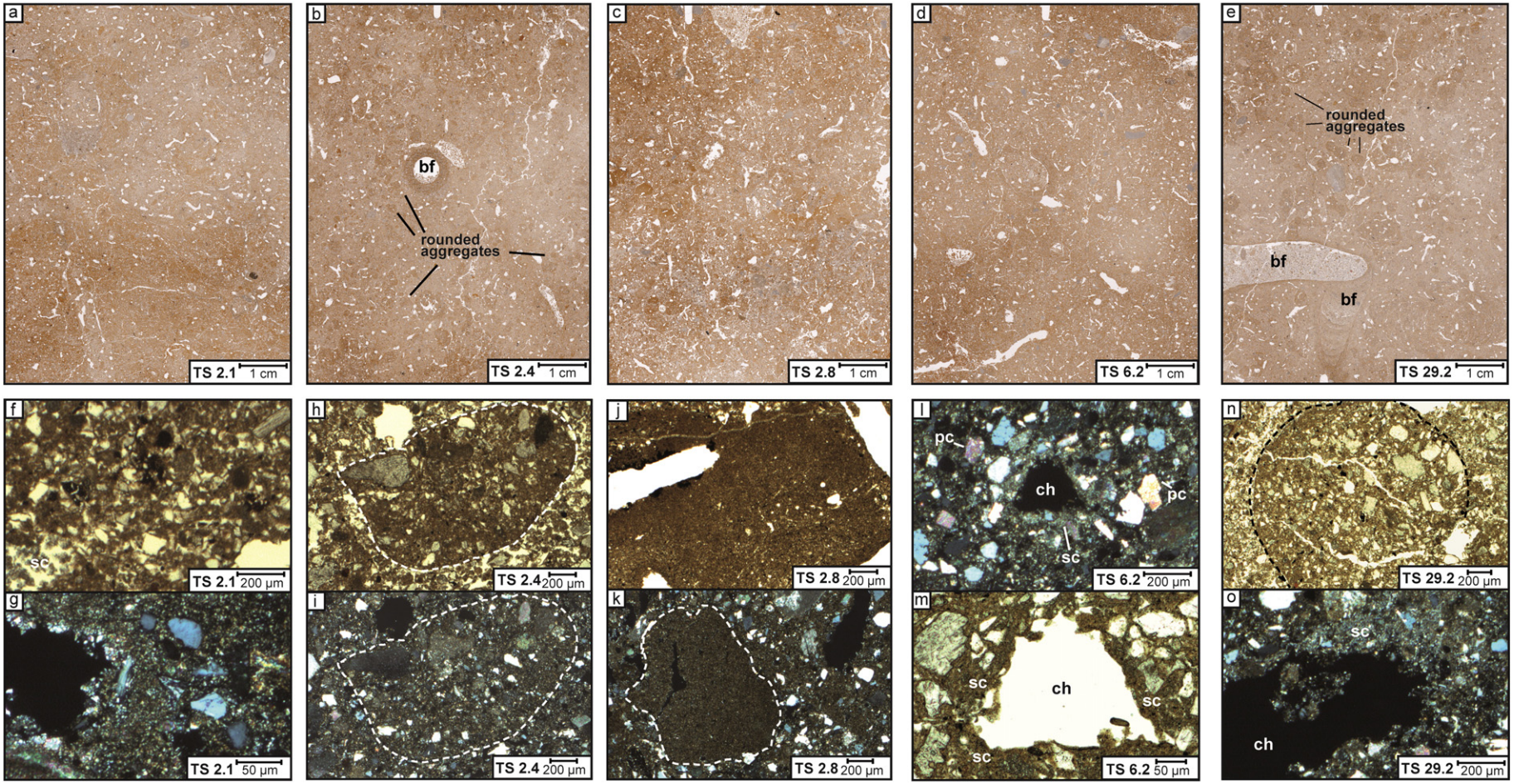

Fig. 9. TS 2.1, 2.4, 2.8, 6.2 and 29.2 associated to TS group 3 (C horizon features). a–e: Flatbed scans showing a high degree of bioturbation in form of chambers and channels, as well as bioturbation features (bf). f: Precipitation of secondary carbonates (sc) along voids under plain-polarised light (PPL). g: Precipitation of secondary carbonates (sc) along voids under crossed-polarised light (XPL). h: (PPL) and i: (XPL) Rounded aggregates are evident, filled by fine-grained material beside rock fragments (borders are marked with white dashed lines). j: Microlayers showing a fining-upward sequence and indicating original fluvial sedimentation (PPL). k: Rounded aggregate filled by fine-grained material (XPL). l: (XPL) and m: (PPL) Hypocoating of secondary carbonate (sc) along one chamber (ch). Coarse-grained rock fragments of primary carbonates (pc) are evident in the matrix. n: Rounded aggregate filled by a mixture of fine- and coarse-grained material originating from the matrix (PPL). o: Slight degree of secondary carbonate (sc) precipitation (XPL). Note that the chamber is not marked by carbonate precipitation.

200 °C was best suited to recover the given dose (0.98 ± 0.05, Fig. 10a), a dominant fast component was presented by CW-OSL component fitting. For the 64 measured multiple-grain aliquots a total of 6 aliquots (~10%) were rejected due to saturation. For single-grain measurements, ~20% of all grains provided bright signals (out of 1400 measured grains) including 106 grains (~38%) with signals above the saturation limit. For D_e determination, 45 multiple-grain aliquots and 40 single grains passed the SAR acceptance criteria. Whilst the multiple-grain data yielded overdispersion >40% (Fig. 10b), the single-grain dose distribution was characterised by even larger scatter (overdispersion >80%; Fig. 10b). The multiple-grain and single-grain dose distributions are approximately symmetrical. Suggesting that sample C-L3828 is affected by post-depositional processes (based on micromorphological analyses; Bk horizon, profile IAM 29), rather than partial bleaching, we used the CAM to calculate a D_e value of 33.7 ± 4.7 Gy and 74.7 ± 6.1 Gy for the single-grain and multiple-grain data set, respectively. The finite mixture model (Galbraith, 2005) was inappropriate for D_e determination due to missing dose populations.

Due to saturation of the quartz signal in most samples, potassium feldspars were also investigated. Sensitivity changes could be corrected adequately, and recuperation was <2% of the sensitivity-corrected natural signal. The prior IR stimulation temperature tests yielded a plateau between 50 and 175 °C for all samples (Fig. 10c). Since intensities of the $pIRIR_{290}$ signal decreased with increasing prior IR temperature and yielded weak signals (Fig. 10d), a prior IR stimulation temperature of 50 °C followed by IR stimulation at 290 °C was used for all feldspar and polymineral samples. Dose recovery ratios between 0.94 ± 0.02 and 1.05 ± 0.03 revealed satisfactory reproducibility (Fig. 10e). Residual doses between ~1 and ~5 Gy (Fig. 10e) and the results of the bleaching experiment of sample C-L3389 (Fig. 10f) indicated adequate resetting of the $pIRIR_{290}$ signal in our samples. Due to rather small residual doses and insignificantly altered D_e, subsequent subtraction from dose recovery and natural doses was redundant. For D_e determination, 13 to 40 aliquots were accepted in case of the feldspar samples, whilst 8 aliquots of the fine-grained polymineral sample C-L3389 passed the SAR criteria. The main reason for rejection was the weak $pIRIR_{290}$ signal. The D_e distributions (Table 3) were characterised by overdispersion values <20%; we applied the CAM for D_e determination for all feldspar and polymineral samples. Fading rates (g-values) of $pIRIR_{290}$ signals (sample C-L3395) varied significantly between aliquots, with values from 0.3 to 1.2%/decade and an average of 0.8 ± 0.4%/decade.

The associated dosimetry data are presented in Table 4. Gamma spectrometric measurements did not yield radioactive disequilibria in the uranium decay chain.

4.4.2. Chronostratigraphy of Wadi Selloums ephemeral stream deposits

All luminescence age estimates are in stratigraphically correct order within each profile. OSL and $pIRIR_{290}$ data are in agreement with age estimates of 13.9 ± 1.0 ka and 12.0 ± 1.1 ka (sample C-L3393), as well as 76 ± 5 ka and 65 ± 6 ka (sample C-L3395), respectively (Fig. 4). Luminescence dating yielded ages dating back to MIS 5c: The five samples from profile IAM 2 yielded $pIRIR_{290}$ ages ranging between 102 ± 8 ka (C-L3389) and 57 ± 4 ka (C-L3830) from base to top (Fig. 3). The lower sample from profile IAM 29 (Fig. 5) yielded an age of 74 ± 6 ka ($pIRIR_{290}$; C-L3829), whilst single-grain and multiple-grain dating of the upper sample (OSL; C-L3828) yielded ages of 18 ± 3 ka and 41 ± 4 ka, respectively.

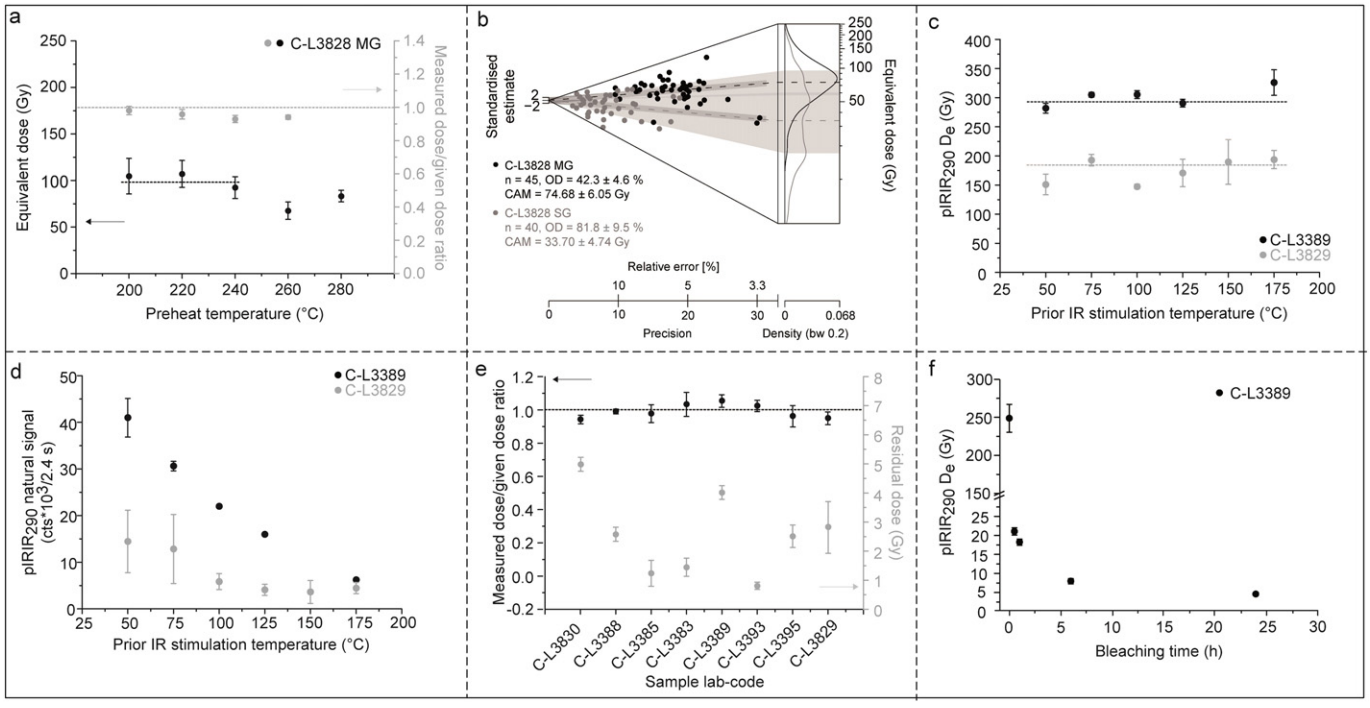

Fig. 10. Luminescence dating results. a: Preheat-plateau (black circles) and dose recovery (grey circles) test results of quartz sample C-L3828 (multiple-grain aliquots). b: Multiple-grain (MG; black circles) and single-grain (SG; grey circles) equivalent dose (D_e) distributions of sample C-L3828 displayed as a combination of a radial plot and a kernel density estimate (KDE) plot (Galbraith and Green, 1990), generated as abanico plot (Dietze et al., 2016). n = number of grains; OD = overdispersion; CAM = central age model (Galbraith et al., 1999). c: Dependence of D_e on prior IR stimulation temperature of sample C-L3389 (fine-grained polymineral) and sample C-L3829 (coarse-grained feldspar); three aliquots were measured. d: Natural $pIRIR_{290}$ signal as a function of the first stimulation temperature (three multiple-grain aliquots, 1 mm). e: Dose recovery results (black circles) and residual doses (grey circles) of all feldspar and polymineral samples; four aliquots were used for both dose recovery and residual dose tests after bleaching in the solar simulator for 24 h. f: Bleaching experiment for sample C-L3389 (fine-grained polymineral; three aliquots for each time).

Table 3
Dose distribution characteristics, equivalent dose (D_e) determinations and age calculations of OSL and $pIRIR_{290}$ samples: SG = single grain; n_a = amount of accepted aliquots (grains); n_m = measured aliquots (grains); OD = overdispersion; CAM = central age model (Galbraith et al., 1999); MAM = minimum age model (Galbraith et al., 1999); n/a = not applicable; * = Bartz et al. (2015).

Profile	Sample ID	Lab. code	Mineral	Grain size (μm)	Aliquot diameter (mm)	n_a/n_m	OD (%)	D_e values (Gy)		Age estimates (ka)	
								CAM	MAM	CAM	MAM
IAM 2	IAM 2-J	C-L3830	Feldspar	100–150	2	21/43	13.7 ± 0.9	139.06 ± 8.21	n/a	56.5 ± 4.4	n/a
	IAM 2-H	C-L3388	Feldspar	100–150	1	13/24	16.5 ± 1.4	166.13 ± 11.49	n/a	72.3 ± 6.4	n/a
	IAM 2-D	C-L3385	Feldspar	100–150	1	14/24	16.2 ± 1.4	169.49 ± 11.46	n/a	73.7 ± 6.4	n/a
	IAM 2-B	C-L3383	Feldspar	100–150	1	20/41	19.2 ± 1.5	177.31 ± 11.91	n/a	74.0 ± 6.5	n/a
	IAM 2-I	C-L3389	Polymineral	4–11	9.8	8/8	2.9 ± 0.3	253.73 ± 13.36	n/a	101.5 ± 8.0	n/a
IAM 6	IAM 6-0	C-L3396	Quartz*	100–150	SG	(50/2640)	67.5 ± 5.8	4.36 ± 0.43	2.23 + 0.16 -0.44	2.6 ± 0.3	1.3 ± 0.2
	IAM 6-1	C-L3390	Quartz*	100–150	1	48/101	26.3 ± 1.4	5.45 ± 0.21	5.16 + 0.35 -0.38	2.5 ± 0.2	2.3 ± 0.2
	IAM 6-2	C-L3391	Quartz*	100–150	1	68/89	15.7 ± 0.6	8.73 ± 0.47	n/a	4.4 ± 0.3	n/a
	IAM 6-3	C-L3392	Quartz*	100–150	1	54/112	13.7 ± 0.5	12.67 ± 0.68	n/a	6.4 ± 0.4	n/a
	IAM 6-4	C-L3393	Quartz*	100–150	1	69/93	17.7 ± 0.7	15.42 ± 0.84	n/a	13.9 ± 1.0	n/a
	IAM 6-4	C-L3393	Feldspar	100–150	1	14/39	7.6 ± 0.5	19.96 ± 1.11	n/a	12.0 ± 1.1	n/a
	IAM 6-5	C-L3395	Quartz*	100–150	1	38/110	15.9 ± 0.8	135.35 ± 3.71	n/a	76.0 ± 4.9	n/a
	IAM 6-5	C-L3395	Feldspar	100–150	1	40/45	15.1 ± 0.7	155.47 ± 8.68	n/a	64.6 ± 5.8	n/a
	IAM 6B1	C-L3544	Quartz*	100–150	1	55/95	13.4 ± 0.5	11.80 ± 0.22	n/a	6.5 ± 0.7	n/a
	IAM 6B2	C-L3545	Quartz*	100–150	1	70/108	14.3 ± 0.5	11.83 ± 0.21	n/a	6.8 ± 0.4	n/a
IAM 29	IAM 29-1	C-L3828	Quartz	100–150	1	45/64	42.3 ± 4.6	74.68 ± 6.05	n/a	41.1 ± 3.7	n/a
	IAM 29-1	C-L3828	Quartz	100–150	SG	(40/1400)	81.8 ± 9.5	33.70 ± 4.74	n/a	18.2 ± 2.7	n/a
	IAM 29-2	C-L3829	Feldspar	100–150	2	34/45	16.0 ± 0.8	174.22 ± 10.07	n/a	73.7 ± 5.6	n/a
Wadi bed	Modern sample	C-L3542	Quartz*	100–150	1	32/100	80.7 ± 9.1	n/a	n/a	n/a	n/a

5. Discussion

5.1. How reliable are the luminescence ages of the ephemeral stream deposits?

The $pIRIR_{290}$ and OSL ages for samples C-L3393 and C-L3395 (Table 3; IAM 6) are in agreement within their 1σ-errors, but show slightly younger feldspar ages implying that our feldspar samples might be affected by anomalous fading. Kars et al. (2014) and Komatsu and Tsukamoto (2015) have mentioned that fading correction in $pIRIR_{290}$ is not redundant. Li and Li (2012) reported D_e underestimation in $pIRIR_{290}$ for samples with high natural doses and recommended an increased temperature up to 200 °C for the prior IR stimulation temperature, which is impossible for the samples of our study due to weak feldspar luminescence signals (Fig. 10d). However, prior IR stimulation temperature tests revealed no influence of anomalous fading. Thus, the prior IR stimulation temperature of 50 °C is able to effectively recombine all electrons stored in traps close enough to recombination centres to have a probability of tunnelling (Buylaert et al., 2012). This is in agreement with our results of the fading experiment which yields an average g-value of 0.8 ± 0.4%/decade. It is, however, rather a laboratory artefact than anomalous fading in nature (Buylaert et al., 2012; Thiel et al., 2011). Thus, we used fading uncorrected feldspar ages for further interpretations. An issue for our feldspars may be the internal dose rate. According to Huntley and Baril (1997), the average internal K content of orthoclase feldspars, based on multiple-grain measurements, is 12.5 ± 0.5%, which was also assumed for K-feldspars in

Table 4
Dose rate data set for quartz and feldspar samples. Summary of radionuclide concentrations of uranium (U), thorium (Th) and potassium (K) determined by high-resolution γ-spectrometry. The DRAC v1.1 (Durcan et al., 2015) was applied for dose rate calculation using the conversion factors of Guérin et al. (2011), and alpha and beta attenuation factors of Bell (1980) and Guérin et al. (2012) (quartz- and feldspar-specific). The contribution of the cosmic dose rate was assessed following the approach of Prescott and Hutton (1994). * = Bartz et al. (2015).

Profile	Sample ID	Lab. code	Mineral	Grain size (μm)	Depth (m b.s.)	Water content (%)	Radionuclide concentration			Dose rate (Gy/ka)	
							U (ppm)	Th (ppm)	K (%)	Cosmic dose rate	Total dose rate
IAM 2	IAM 2-J	C-L3830	Feldspar	100–150	0.90	15 ± 5	1.69 ± 0.09	6.05 ± 0.36	1.11 ± 0.01	0.19 ± 0.02	2.46 ± 0.12
	IAM 2-H	C-L3388	Feldspar	100–150	1.90	15 ± 5	1.50 ± 0.10	5.57 ± 0.41	1.05 ± 0.06	0.16 ± 0.02	2.29 ± 0.13
	IAM 2-D	C-L3385	Feldspar	100–150	2.85	15 ± 5	1.57 ± 0.08	5.60 ± 0.33	1.06 ± 0.04	0.14 ± 0.01	2.30 ± 0.12
	IAM 2-B	C-L3383	Feldspar	100–150	3.85	20 ± 6	1.69 ± 0.12	6.39 ± 0.46	1.20 ± 0.07	0.12 ± 0.01	2.39 ± 0.14
	IAM 2-I	C-L3389	Polymineral	4–11	4.80	20 ± 6	1.78 ± 0.12	6.70 ± 0.48	1.30 ± 0.07	0.10 ± 0.01	2.50 ± 0.15
IAM 6	IAM 6-0	C-L3396	Quartz*	100–150	0.15	4 ± 1	1.22 ± 0.09	4.16 ± 0.30	0.92 ± 0.05	0.26 ± 0.03	1.68 ± 0.10
	IAM 6-1	C-L3390	Quartz*	100–150	0.45	9 ± 3	1.77 ± 0.12	6.39 ± 0.46	1.38 ± 0.08	0.22 ± 0.02	2.22 ± 0.13
	IAM 6-2	C-L3391	Quartz*	100–150	1.05	11 ± 4	1.63 ± 0.08	5.73 ± 0.33	1.28 ± 0.05	0.19 ± 0.02	1.99 ± 0.16
	IAM 6-3	C-L3392	Quartz*	100–150	1.50	6 ± 2	1.49 ± 0.10	5.62 ± 0.41	1.22 ± 0.07	0.17 ± 0.02	1.98 ± 0.10
	IAM 6-4	C-L3393	Quartz*	100–150	2.42	5 ± 1	0.90 ± 0.06	2.83 ± 0.21	0.61 ± 0.04	0.15 ± 0.02	1.11 ± 0.08
	IAM 6-4	C-L3393	Feldspar	100–150	2.42	5 ± 1	0.90 ± 0.06	2.83 ± 0.21	0.61 ± 0.04	0.15 ± 0.02	1.66 ± 0.10
	IAM 6-5	C-L3395	Quartz*	100–150	4.50	12 ± 4	1.39 ± 0.10	5.88 ± 0.43	1.18 ± 0.07	0.11 ± 0.01	1.76 ± 0.12
	IAM 6-5	C-L3395	Feldspar	100–150	4.50	12 ± 4	1.39 ± 0.10	5.88 ± 0.43	1.18 ± 0.07	0.11 ± 0.01	2.41 ± 0.13
	IAM 6B1	C-L3544	Quartz*	100–150	1.65	4 ± 1	1.41 ± 0.21	4.94 ± 0.36	1.05 ± 0.06	0.17 ± 0.02	1.80 ± 0.09
	IAM 6B2	C-L3545	Quartz*	100–150	1.65	4 ± 1	1.38 ± 0.10	4.67 ± 0.34	1.01 ± 0.06	0.17 ± 0.02	1.73 ± 0.08
IAM 29	IAM 29-1	C-L3828	Quartz	100–150	0.90	10 ± 3	1.33 ± 0.07	5.41 ± 0.33	1.12 ± 0.01	0.20 ± 0.02	1.83 ± 0.05
	IAM 29-2	C-L3829	Feldspar	100–150	1.97	12 ± 4	1.60 ± 0.09	5.77 ± 0.35	1.02 ± 0.01	0.16 ± 0.02	2.36 ± 0.12
Wadi bed	Modern sample	C-L3542	Quartz*	100–150	0.10	4 ± 1	0.65 ± 0.05	1.60 ± 0.13	0.32 ± 0.02	0.26 ± 0.03	0.82 ± 0.06

the Wadi Selloum catchment. Based on single-grain feldspar measurements, Reimann et al. (2012) have shown a dependence between the luminescence intensity and the internal K content. Hence, only the brightest grains have an average K content of 12.5%, whilst the dimmer grains may contain less K (Reimann et al., 2012). A lot of feldspar multiple-grain aliquots were rejected due to weak luminescence signals. Following Reimann et al. (2012) this may hint to overestimated dose rates due to generally dim feldspar grains within the multiple-grain aliquots. However, measurements of individual potassium concentrations are not available for our samples, therefore using an assumed potassium concentration of 12.5 ± 0.5% seems to be the best way to calculate the dose rate.

Insufficient bleaching prior to final deposition is a common bias resulting in age overestimation of fluvial deposits (e.g. Wallinga, 2002). First investigations on modern quartz samples collected in the Wadi Selloum catchment showed that partial bleaching influenced samples with residual doses as high as 46 Gy (Bartz et al., 2015). This is not necessarily redundant for older samples, but with a mean residual dose of ~11 Gy it should influence especially the younger samples (Bartz et al., 2015; Jain et al., 2004; Murray et al., 2012). Overall agreement of quartz and feldspar ages indicates that both luminescence signals are able to date the true burial age of the ephemeral stream deposits. Since the time required for complete resetting of the $pIRIR_{290}$ signal is much longer than that of the OSL signal, this convergence is only possible when both luminescence signals are well bleached before deposition (Murray et al., 2012; Thomsen et al., 2016).

Post-depositional processes were observed in our micromorphological studies (TS group 2; Fig. 8) which confirm biological activity (e.g. passage features) that leads to sediment mixing. These post-depositional processes and processes during deposition (i.e. partial resetting of the luminescence signal) should be carefully considered for luminescence samples with large scatter in the D_e distribution (Bateman et al., 2003; Murray et al., 2012). Sample C-L3828, collected in a Bk horizon (Fig. 5), shows significant scatter in the quartz D_e distribution when using both small aliquots (1 mm) and single grains (Fig. 10b). We interpret that the large D_e scatter derives mainly from post-depositional processes in the sediment layer. Therefore, the minimum age model (Galbraith et al., 1999) is not suitable for D_e determination, since bioturbated samples might be contributed by low and high D_e values, in contrast to partially bleached samples (Bartz et al., 2015; Bateman et al., 2007). When comparing our single-grain CAM dose to that of the multiple-grain CAM dose, then the single-grain dose systematically underestimates the multiple-grain dose, which is similar to investigations of Thomsen et al. (2016). In the single-grain data set, ~38% of all grains yielded OSL signals in saturation, which might be the result of transported grains from lower sediment horizons. On the one hand, the use of multiple-grain aliquots might not be appropriate, since single grains with high doses contribute to the cumulative light sum of multiple-grain aliquots which would be rejected on the single-grain base. In this case the true burial age might be overestimated when using multiple-grain aliquots. On the other hand, it is still questionable whether the single-grain dose is underestimated due to many rejected saturated grains. Bearing in mind that an age cross-check does not exist for sample C-L3828, we carefully interpret that the CAM dose might give us a burial age of 18 ± 3 ka on the single-grain base (Table 3), but should rather be considered as minimum age. It should also be taken with caution that the sampling location of sample C-L3828 (profile IAM 29; unit 5; Fig. 5) is affected by carbonate movements over time. Precipitation of secondary carbonates in the Bk horizon influences the external dose rate which is thus not constant since burial due to carbonate replacements of water and air in the sediment pores (Nathan and Mauz, 2008).

Luminescence dating of ephemeral stream sediments still remains challenging due to complex luminescence characteristics. Although independent age control was not available to cross-check our luminescence results in the Wadi Selloum, thorough laboratory experiments and inter-method comparisons between OSL and $pIRIR_{290}$ allow for establishing a reliable chronology of the Wadi Selloum deposits.

5.2. Pedogenetic features in ephemeral stream deposits of Wadi Selloum

Soil forming processes are observed in the Wadi Selloum deposits and may serve as environmental marker to detect landscape changes (Eppes et al., 2008). The accumulation or translocation of secondary carbonates are obvious in the three identified soils in our study. Channel or chamber microstructures reflect biological activity in the form of root growth and soil mesofauna. Mammilated or spherical and often elongated mineral excrements of high packing density and slightly reddish-brown colour resemble earthworm casts of *Lumbricidae* (Stoops, 2003). Aldeias et al. (2014) observed similar excrements in Last Glacial deposits of the Contrebandiers Cave (Western coast of Morocco), and related them to earthworms. Earthworm calcite was not detected in thin sections of our study. Therefore, it is still unclear, which type of soil-dwelling mesofauna produced these excrements. It is likely that the circular to ellipsoid burrows, showing well-formed walls and defined as sediment cocoons, were built by solitary wasp, as also suggested by Aldeias et al. (2014) for similar burrows at Contrebandiers Cave. Moreover, weakly expressed redoximorphic features such as Fe and Mn nodules are further indicators of pedogenesis. Formation of these features is mediated by microbial reduction of Fe and Mn in the presence of organic matter under reducing conditions and precipitation as oxides in the presence of oxygen, for instance under the influence of water table fluctuations (Lindbo et al., 2010).

During the late Holocene a weak Fluvisol (soil II) developed in profile IAM 6, whilst earlier pedogenesis is evident from the well-preserved Calcisol (soil I) in profiles IAM 28 and IAM 29 that developed during the mid- and early Holocene. The palaeosol in profiles IAM 28 and IAM 29 shares common features with the Calcisol (Bk horizon), but developed during the Late Pleistocene. Similarly, Badía et al. (2015) have shown that in semiarid NE Spain young soils of the Late Holocene are Calcaric Fluvisols and older soils developed since the Holocene-Pleistocene boundary are Haplic Calcisols. Nevertheless, changes of pedogenic properties over time cannot be regularly age-related due to the variability of the climate along the Late Pleistocene (Badía et al., 2009). The older Calcisol (palaeosol) post-dates 74 ± 6 ka ($pIRIR_{290}$; C-L3829) and indicates the oldest recorded soil in the Wadi Selloum deposits. The palaeosol sequence was only captured in two profiles, illustrating the high variability in degradation and aggradation processes of such ephemeral stream systems (Bull, 1997). Yet, information about pedogenesis during MIS 3 are not documented in terrestrial archives from NE Morocco. Eppes et al. (2008) have suggested that pedogenic carbonate precipitates during drier climates and is susceptible to dissolution during wetter periods in Italy. In Southern Spain, García-García et al. (2016) have shown Calcisol development between >44 and 34 ka due to more humid climate conditions.

5.3. Morphodynamic phases during the last 100 ka

Based on sediment characteristics and luminescence ages, chronostratigraphies for the four profiles are proposed (Fig. 11), and observed similarities between profiles are referred to as layers in the following.

5.3.1. Layer I – oldest channel deposits

Given its age (>74 ± 6 ka) and its high degree of solidification, we suggest that the lowermost gravel layer I (C1) of profiles IAM 28 and IAM 29 might represent the oldest channel deposits of Wadi Selloum

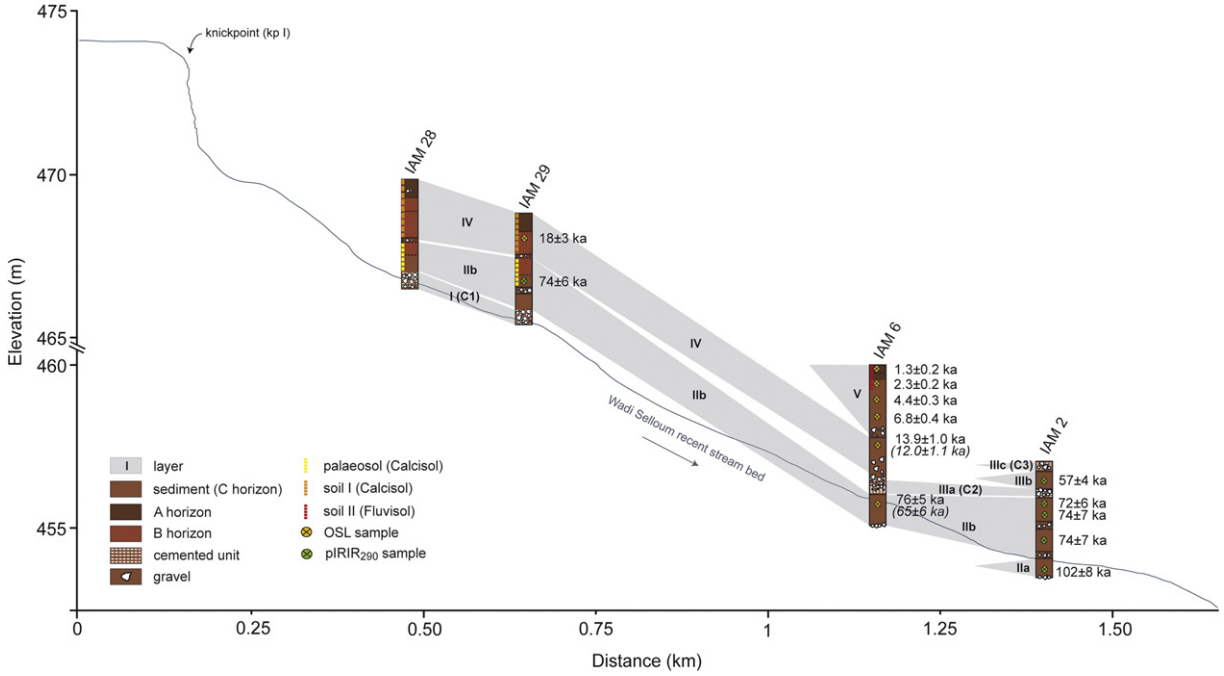

Fig. 11. Correlation of sedimentary layers of the studied profiles IAM 2, IAM 6, IAM 28 and IAM 29. In profile IAM 6 two samples were dated by OSL and $pIRIR_{290}$ for an inter-method comparison; the $pIRIR_{290}$ ages are presented in brackets.

(Figs. 5, 6). Similar observations were reported from a wadi system in Jordan, where variable degrees of carbonate cementation affected younger and older channel deposits (i.e. channel calcretes; McLaren, 2004). The absence of layer I in profile IAM 2 (dated to 102 ± 8 ka at its base) underlines the longitudinal discontinuity of ephemeral stream deposits (Bull, 1997). Such systems are characterised by significant channel changes over time, particularly related to the occurrence of high-energy flash floods (Patton and Schumm, 1981; Poesen and Hooke, 1997), as demonstrated by intense morphological changes during six decades in ephemeral stream channels of eastern Spain (Segura-Beltrán and Sanchis-Ibor, 2013).

5.3.2. Layer II – ephemeral stream deposits around 100 ka and 75 ka

The fine-grained sediments (layer II) can be subdivided in layers IIa and IIb with luminescence ages of ~100 (MIS 5c) and ~75 ka (MIS 5a), respectively. Whilst layer IIa is only observed in profile IAM 2 (Fig. 3), the silty/clay-rich layer IIb is evident in all profiles and seems thus pointing to enhanced aggradation during MIS 5a. It is characterised by a large amount of local material (carbonate, dolomite) and a minor component of allochthonous aeolian sediments (quartz, K-feldspar, plagioclase). It is not straightforward to correlate these massive, unstratified ~2.50 m-thick deposits in profile IAM 2 with one or several flooding event(s) around 75 ka. Contrary to coarse-grained gravels, fine-grained sediments (silts/clays) might also have been transported by hillslope processes and not deposited as overbank sediments (Bull, 1997; Patton and Schumm, 1981). Increasing stabilisation of the land surface by vegetation, confirmed by the development of the palaeosol (Calcisol), may have led to enhanced sedimentation of finer sediments (Sandercock et al., 2007).

5.3.3. Layer III – palaeochannel features and overbank aggradation around 55 ka

In profile IAM 2, the cemented layers IIIa (C2) and IIIc (C3) show similar characteristics to channel calcretes described in the Tabernas Basin in SE Spain (Nash and Smith, 2003). The active stream bed of Wadi Selloum at knickpoints kp I and kp II revealed dm-thick $CaCO_3$-cemented layers at the base of gravel deposits (Fig. 2a, b). The development of these calcretes seems closely related to along-channel subsurface waters, extremely rich in carbonate, originating from the local Mesozoic rocks (Benjelloun et al., 1971). The assumption of geomorphologically stable surfaces and enhanced pedogenetic processes with subsequent calcrete development for C2 and C3 seems unrealistic because these rather thin calcretes show no evidence of hardpan formation (Candy et al., 2003). We therefore assume that layers C2 and C3 correspond to palaeochannels, located higher in the stratigraphic sequence than the present stream bed: +2.50 m (C2) and +4.0 m (C3), with respective aggradation periods of ~72 ka/~55 ka and <55 ka. Apparently, only sediments from the beginning of MIS 3 could be identified in profile IAM 2, whilst other investigated profiles do not show characteristics of MIS 3 deposits.

5.3.4. Layer IV – aggradation around 15 ka

After a phase of morphodynamic stability attested by the palaeosol (Calcisol; layer II; profiles IAM 28 and IAM 29), the layer IV is visible in profiles IAM 6, IAM 28 and IAM 29 (Fig. 11), reflecting enhanced aggradation which took place at least between 18 ± 3 ka and 13.9 ± 1.0 ka (Bartz et al., 2015). It is characterised by coarse silt to fine sand particles and high contents of allochthonous minerals (quartz, K-feldspar and plagioclase), which may suggest that aeolian input increased during MIS 2. Profile IAM 6 presents an erosional disconformity of coarser sediments (unit 3; Fig. 4), indicating enhanced hillslope deposition, characterised by unsorted angular deposits, after ~14 ka.

5.3.5. Layer V – Holocene aggradation, landscape stability and recent incision

Only represented in profile IAM 6, the Holocene sequence between 6.8 ± 0.4 ka and 1.3 ± 0.2 ka (layer V, Figs. 4, 11) seems to display relative stability of the landscape and subsequent sediment trapping (Sandercock et al., 2007). The weakly developed Fluvisol (soil II) in the upper part of profile IAM 6 reflects the development of a stable land surface during the late Holocene, at least since ~1.3 ka. Afterwards, fluvial incision seems to be the dominant process in the catchment. Nowadays, the landscape is only covered by sparse vegetation due to intensive anthropogenic land use, which, in turn, induces soil degradation and erosion. This might have been the main reason for enhanced incision during recent times.

5.4. Correlation with the archaeological sequence of Ifri n'Ammar and Late Quaternary palaeoenvironmental records of the Western Mediterranean region

The chronostratigraphies of the ephemeral stream deposits and of the archaeological sequence of Ifri n'Ammar are both discontinuous and span the time periods comprised between 102 ± 8 to 1.3 ± 0.2 ka (Table 3) and 171 ± 12 ka to 11.7 ± 0.4 cal ka BP (Nami and Moser, 2010; Richter et al., 2010), respectively. Fig. 12 summarises the correlation between morphodynamic phases of Wadi Selloum, the archaeological data of Ifri n'Ammar (Linstädter et al., 2012; Nami and Moser, 2010) as well as palaeoclimate records retrieved off the coast of West Africa as well as in the Alboran Sea and the Aegean Sea (Ehrmann et al., 2013; Pérez-Folgado et al., 2004; Tjallingii et al., 2008).

5.4.1. MIS 5

The deposition of layer II correlates with MIS 5c (IIa) and MIS 5a (IIb). Given the uncertainty affecting both the TL ages of the archaeological sequence and our luminescence ages, layer II only matches the Middle Palaeolithic period around 83 ± 6 ka in Ifri n'Ammar (Nami and Moser, 2010; Richter et al., 2010). MIS 5c and MIS 5a are marked by warmer conditions in the Alboran Sea (Pérez-Folgado et al., 2004). Additionally, two distinct African Humid Periods (AHP) are attested during MIS 5c (>105–95 ka; Ehrmann et al., 2013) and MIS 5a (83.5–72 ka; Ehrmann et al., 2013) characterised by a more humid climate and enhanced precipitation (Ehrmann et al., 2013). Such warm and humid conditions can be seen as favourable for human occupation, somehow verified by extensive findings of Middle Palaeolithic artefacts in Ifri n'Ammar (Nami and Moser, 2010). Likewise, MIS 5 appears to be an intense period of AMH settling in coastal areas of Morocco (e.g. Campmas et al., 2015).

5.4.2. MIS 4–MIS 3

From the four investigated profiles, only one luminescence age points to MIS 4–MIS 3 (profile IAM 2). In parallel to this time period during which little aggradation is observed in our ephemeral stream system, few information is available for the final stage of the Middle Palaeolithic and the early Upper Palaeolithic in Ifri n'Ammar. This

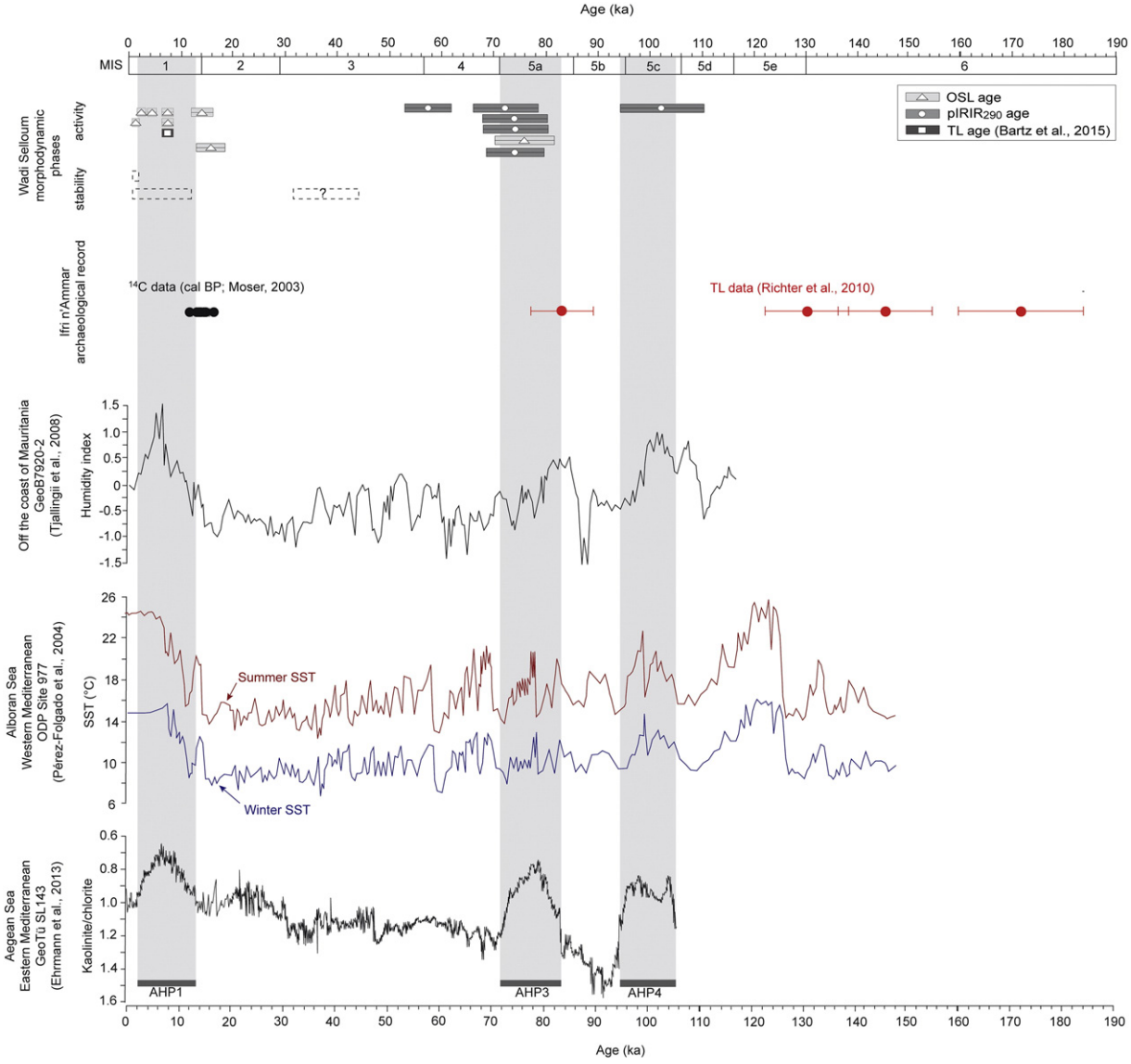

Fig. 12. Correlation between morphodynamic phases of Wadi Selloum, archaeological data of Ifri n'Ammar (Moser, 2003; Richter et al., 2010), as well as palaeoclimate records from the Mediterranean region (Ehrmann et al., 2013; Pérez-Folgado et al., 2004; Tjallingii et al., 2008). MIS = marine isotope stage; AHP = African humid period.

might indicate that human occupation in this region declined between ~50 ka and the end of Heinrich Event (HE) 2 around 24 ka (Linstädter et al., 2012). Tjallingii et al. (2008) have described MIS 4 as an arid period. Also, a higher supply of aeolian material in the Mediterranean from the North African deserts indicates drier conditions (Ehrmann et al., 2013). Additionally, the coldest sea surface temperatures occurred during MIS 4, especially around 60 ka (Pérez-Folgado et al., 2004). MIS 3 is characterised by climatic variations linked to North Atlantic HE and Dansgaard-Oeschger (D/O) cycles reflected by several proxy records of marine sediments from the Alboran Sea (Moreno et al., 2002; Moreno, 2012). Tjallingii et al. (2008) have mentioned abrupt millennial-scale alternations of arid and humid events during MIS 3. Other fluvial records from the Iberian Peninsula have shown that river sediments of MIS 4 and MIS 3 are usually not observed (Santisteban and Schulte, 2007). Due to the development of the palaeosol post-dating 74 ± 6 ka (Fig. 5), increased stabilisation of the land surface together with enhanced vegetation growth may be assumed, probably during MIS 3, when more humid conditions prevailed.

5.4.3. MIS 2

The aggradation time span of layer IV (at least 18 ± 3 ka to 13.9 ± 1.0 ka) fairly well matches the period of the Iberomaurusian culture in north-western Africa (Linstädter et al., 2012), particularly well represented in the archaeological sequence of Ifri n'Ammar (Moser, 2003; Nami and Moser, 2010). In the latter, this culture was characterised by mollusc consumption during the Bølling-Allerød interstadial period (Zielhofer, 2007). Based on fluvial archives of the lower Kert River (Fig. 1a), which include deposits from the Bølling-Allerød and the Younger Dryas (Barathon et al., 2000), El Amrani et al. (2008) inferred a cool and humid (partly arid) climate after 30 ka BP, mainly characterised by sediment aggradation. A highly consistent picture of river activity is evidenced across the Mediterranean basin during MIS 2 (Macklin et al., 2002). This is in agreement with other fluvial basins in the Mediterranean (Santisteban and Schulte, 2007).

5.4.4. Holocene

The middle to late Holocene aggradation recorded in layer V (6.8 ± 0.4 ka to 1.3 ± 0.2 ka, Fig. 11) is concomitant with the Neolithic period, which is not represented in the archaeological sequence. However, numerous Neolithic traces are observed in the entrance talus of the cave, and confirmed by a TL-dated pottery shard (7.4 ± 0.6 ka) extracted from the profile IAM 6 (Bartz et al., 2015). The onset of the Neolithic period in this region was related to the Mediterranean climate optimum around 7.5 ka (Zielhofer and Linstädter, 2006). However, the more humid Neolithic period seems to have been interrupted by a more arid event around 6–5 cal ka BP (Fletcher and Zielhofer, 2013). The perennial Kert River reflects high aggradation rates in mid- to late Holocene times (El Amrani et al., 2008). This is in agreement with Zielhofer et al. (2010), who reported flood activity in the Lower Moulouya River particularly during an arid event between 3.2 and 2.7 cal ka BP. This short climatic event is also reflected in the alluvial sequences of the Medjerda River in Tunisia (Faust et al., 2004).

Channel-parallel layering of terrestrial gastropods (e.g. *Otala* cf. *lactea*) and charcoal remains around 2.3 ± 0.2 ka (Fig. 4) might point to a palaeo-surface. It was, however, not long enough stable for a pronounced soil formation, as evidenced by the sparsity of pedofeatures visible in TS 6.1 and preserved stratification of the Fluvisol (layer V of profile IAM 6; Fig. 4). Therefore, we assume that Wadi Selloum was affected by short-term environmental changes during the late Holocene. Flood variability during that time range is also reported for the rivers Moulouya and Kert (Benito et al., 2015; El Amrani et al., 2008; Ibouhouten et al., 2010; Zielhofer et al., 2010). From marine palaeoclimate records (Fig. 12), an African Humid Period was observed between 14 and 2 ka (Ehrmann et al., 2013). These records would suggest fluvial activity during more humid climate conditions in Wadi Selloum. After ~1.3 ka, the sedimentation appears to have ended in Wadi Selloum. Similar observations were reported from the terrace sequences of the Kert River (El Amrani et al., 2008) and the Moulouya River (Zielhofer et al., 2010).

Since AMH have settled in the vicinity of Ifri n'Ammar for many millennia, human impact on fluvial morphodynamics of Wadi Selloum, though difficult to quantify, may have played a significant role. In particular, the transition of hunter-gatherer communities to agricultural activity resulted in an intensified agricultural land-use that may have triggered soil erosion (Linstädter et al., 2012), which, in turn, activated geomorphologic erosional processes. In southern Morocco, the beginning of the Islamic period around 1.3 ka BP led to expanded pastoralism, deforestation and agriculture, which changed the vegetation structure (McGregor et al., 2009). Schulte (2003) reported that human impact on river dynamics in the Vera and Penedes basins in Spain may have been crucial with respect to magnitude of surface runoff and sedimentation.

6. Summary and conclusion

The discontinuity of ephemeral stream systems underlines the difficulties for interpreting morphodynamic phases in Wadi Selloum. The application of luminescence dating techniques (OSL, $pIRIR_{290}$, TL; see also Bartz et al., 2015) has established for the first time a geochronological framework for ephemeral stream deposits in NE Morocco. Thus, a well-dated ephemeral stream archive is presented, which supports the reconstruction of wadi morphodynamics. The depositional ages for the Wadi Selloum sediment sections show aggradation during MIS 5c and MIS 5a, as well as from after the LGM to the Bølling-Allerød period, and the Holocene. Morphodynamic activity of Wadi Selloum may be linked to humid periods (African Humid Periods: >105–95, 83.5–72 and 14–2 ka; Ehrmann et al., 2013), but should be taken with caution due to the high discontinuity of the studied archive and the uncertainties of the luminescence ages. Pedogenesis may be used as significant environmental marker, indicating more humid climate conditions in form of secondary carbonate precipitation during MIS 3 (Calcisol; palaeosol), since early Holocene times (Calcisol; soil I) and the late Holocene (Fluvisol; soil II).

Nevertheless, the reconstruction of the palaeo-landscape is still challenging due to the high erosional power of the complex ephemeral stream system. A single high-energy flash flood event can cause a significant gap in the sediment archive, which then leads to a discontinuous record. Due to the complexity of the given ephemeral stream system, it is difficult to establish a linkage between the occupation phases of the rock shelter of Ifri n'Ammar on the one hand, and environmental changes on the other hand.

Our data correspond to the time of the Middle Palaeolithic and the Iberomaurusian culture and provide first insights into palaeoenvironmental changes around Ifri n'Ammar. The question whether humans occupied Ifri n'Ammar during warm/wet or cold/dry climate conditions remains open; however, our data may suggest that humans occupied Ifri n'Ammar during wetter and warmer climatic conditions.

Acknowledgements

This project is part of the CRC 806 “Our Way to Europe”, which is funded by the *German Research Foundation* (*DFG*) (ref. no. SFB 806/2). The support by the *Institut National des Sciences de l'Archéologie et du Patrimoine du Maroc* (*INSAP*) and by the *Commission for Archaeology of Non-European Cultures* (*KAAK*) of the *German Archaeological Institute* (*DAI*), in particular Josef Eiwanger, is gratefully acknowledged. We thank Rainer Hutterer, Bonn, for his help in the determination of terrestrial gastropods, and Nina Szemkus, Cologne, for her commitment to this project. Three anonymous reviewers are acknowledged for their constructive comments that helped to improve the manuscript.

References

Abdalla, F., El Shamy, I., Bamousa, A.O., Mansour, A., Mohamed, A., Tahoon, M., 2014. Flash floods and groundwater recharge potentials in arid land alluvial basins, southern Red Sea coast, Egypt. Int. J. Geosci. 5, 971–982.

Aldeias, V., Goldberg, P., Dibble, H.L., El-Hajraoui, M., 2014. Deciphering site formation processes through soil micromorphology at Contrebandiers Cave, Morocco. J. Hum. Evol. 69, 8–30.

Auclair, M., Lamothe, M., Huot, S., 2003. Measurement of anomalous fading for feldspar IRSL using SAR. Radiat. Meas. 37, 487–492.

Badía, D., Martí, C., Palacio, E., Sancho, C., Poch, R.P., 2009. Soil evolution over the Quaternary period in a semiarid climate (Segre river terraces, northeast Spain). Catena 77, 165–174.

Badía, D., Martí, C., Casanova, J., Gillot, T., Cuchi, J.A., Palacio, J., Andrès, R., 2015. A Quaternary soil chronosequence study on the terraces of the Alcanadre River (semiarid Ebro basin, NE Spain). Geoderma 241–242, 158–167.

Balescu, S., Lamothe, M., 1993. Thermoluminescence dating of the Holsteinian marine formation of Herzeele, northern France. J. Quat. Sci. 8 (2), 117–124.

Barathon, J.-J., El Abassi, H., Lechevalier, C., Malek, F., Jolly-Saad, M.-C., 2000. Mise au point sur les formations holocènes dans le Rif oriental (Maroc)/A chronology of Holocene deposits in the eastern Rif Mountains (Morocco). Géomorphologie 6 (4), 221–238.

Barcos, L., Jabaloy, A., Azdimousa, A., Asebriy, L., Gómez-Ortis, D., Rodríguez-Peces, M.J., Tejero, R., Pérez-Peña, J.V., 2014. Study of relief changes related to active doming in the eastern Moroccan Rif (Morocco) using geomorphological indices. J. Afr. Earth Sci. 100, 493–509.

Barton, R.N.E., Bouzouggar, A., Collcutt, S.N., Gale, R., Higham, T.F.G., Humphrey, L.T., Parfitt, S., Rhodes, E., Stringer, C.B., Malek, F., 2005. The late upper palaeolithic occupation of the Moroccan northwest Maghreb during the last glacial maximum. Afr. Archaeol. Rev. 22 (2), 77–100.

Bartz, M., Klasen, N., Zander, A., Brill, D., Rixhon, G., Seeliger, M., Eiwanger, J., Weniger, G.-C., Mikdad, A., Brückner, H., 2015. Luminescence dating of ephemeral stream deposits around the palaeolithic site of Ifri n'Ammar (Morocco). Quat. Geochronol. 30, 460–465.

Bateman, M.D., Frederick, C.D., Jaiswal, M.K., Singhvi, A.K., 2003. Investigations into the potential effects of pedoturbation on luminescence dating. Quat. Sci. Rev. 22, 1169–1176.

Bateman, M.D., Boulter, C.H., Carr, A.S., Frederick, C.D., Peter, D., Wilder, M., 2007. Detecting post-depositional sediment disturbance in sandy deposits using optical luminescence. Quat. Geochronol. 2, 57–64.

Beckmann, T., 1997. Präparation bodenkundlicher Dünnschliffe für mikromorphologische Untersuchungen. Hohenheimer Bodenkundliche Hefte. 40, pp. 89–103.

Bell, W.T., 1980. Alpha dose attenuation in quartz grains for thermoluminescence dating. Ancient TL 12, 4–8.

Benito, G., Macklin, M.G., Zielhofer, C., Jones, A.F., Machado, M.J., 2015. Holocene flooding and climate change in the Mediterranean. Catena 130, 13–33.

Benjelloun, S.E., Douïeb, M., Saadi, M., Ennadifi, Y., 1971. Carte Géologique du Maroc. 167, 1:100000, Tistoutine.

Bertrams, M., Protze, J., Löhrer, R., Schyle, D., Richter, J., Hilgers, A., Klasen, N., Schmidt, C., Lehmkuhl, F., 2012. Multiple environmental change at the time of the modern human passage through the Middle East – first results from geoarchaeological investigations on upper Pleistocene sediments in the Wadi Sabra (Jordan). Quat. Int. 274, 55–72.

Blott, S.J., Pye, K., 2001. GRADISTAT: a grain size distribution and statistics package for the analysis of unconsolidated sediments. Earth Surf. Process. Landf. 26, 1237–1248.

Boski, T., Pessoa, J., Pedro, P., Thorez, J., Dias, J.M.A., Hall, I.R., 1998. Factors governing abundance of hydrolysable amino acids in the sediments from the NW European continental margin (47–50°N). Prog. Oceanogr. 42, 145–164.

Bøtter-Jensen, L., Bulur, E., Duller, G.A.T., Murray, A.S., 2000. Advances in luminescence instrument systems. Radiat. Meas. 32, 523–528.

Bubenzer, O., Hilgers, A., Riemer, H., 2007. Luminescence dating and archaeology of Holocene fluvio-lacustrine sediments of Abu Tartur, eastern Sahara. Quat. Geochronol. 2, 317–321.

Bull, W.B., 1997. Discontinuous ephemeral streams. Geomorphology 19, 227–276.

Buylaert, J.-P., Jain, M., Murray, A.S., Thomsen, K.J., Thiel, C., Sohbati, R., 2012. A robust feldspar luminescence dating method for middle to late Pleistocene sediments. Boreas 41, 435–451.

Campmas, E., Michel, P., Costamagno, S., Amani, F., Stoetzel, E., Nespoulet, R., El Hajraoui, M.A., 2015. Were upper Pleistocene human/non-human predator occupations at the Témara caves (El Harhoura 2 and El Mnasra, Morocco) influenced by climate change? J. Hum. Evol. 78, 122–143.

Candy, I., Black, S., Sellwood, B.W., Rowan, J.S., 2003. Calcrete profile development in Quaternary alluvial sequences, southeast Spain: implications for using calcretes as a basis for landform chronologies. Earth Surf. Process. Landf. 28, 169–185.

Cook, H.E., Johnson, P.D., Matti, J.C., Zemmels, I., 1975. Methods of sample preparation and X-ray diffraction analysis in x-ray mineralogy laboratory. In: Kaneps, A.G., et al. (Eds.), Init. Rep. DSDP XXVIII. Printing Office, Washington, DC, pp. 997–1007.

Courty, M.-A., Vallverdu, J., 2001. The microstratigraphic record of abrupt climate changes in cave sediments of the western Mediterranean. Geoarchaeology 16 (5), 467–500.

Dietze, M., Kreutzer, S., Burow, C., Fuchs, M.C., Fischer, M., Schmidt, C., 2016. The abanico plot: visualising chronometric data with individual standard errors. Quat. Geochronol. 31, 12–18.

Duller, G.A.T., 2003. Distinguishing quartz and feldspar in single grain luminescence measurements. Radiat. Meas. 37, 161–165.

Durcan, J.A., King, G.E., Duller, G.A.T., 2015. DRAC: dose rate and age calculator for trapped charge dating. Quat. Geochronol. 28, 54–61.

Ehrmann, W., Seidel, M., Schmiedl, G., 2013. Dynamics of late Quaternary North African humid periods documented in the clay mineral record of central Aegean Sea sediments. Glob. Planet. Chang. 107, 186–195.

El Amrani, M., Macaire, J.-J., Zarki, H., Bréhéret, J.-G., Fontugne, M., 2008. Contrasted morphosedimentary activity of the lower Kert River (northeastern Morocco) during the late Pleistocene and the Holocene. Possible impact of bioclimatic variations and human action. Compt. Rendus Geosci. 340, 533–542.

Eppes, M.C., Bierma, R., Vinson, D., Pazzaglia, F., 2008. A soil chronosequence study of the Reno valley, Italy: insights into the relative role of climate versus anthropogenic forcing on hillslope processes during the mid-Holocene. Geoderma 147, 97–107.

Esri, 2014. DigitalGlobe, Earthstar Geographics, CNES/Airbus DS, GeoEye, USDA FSA, USGS, Getmapping, Aerogrid, IGN, IGP, Swisstopo, and the GIS User Community.

FAO; Food and Agriculture Organization of the United Nations, 2006n. Guidelines for Soil Description. fourth ed. Rome.

Faust, D., Zielhofer, C., Baena Escudero, R., Diaz del Olmo, F., 2004. High-resolution fluvial record of late Holocene geomorphic change in northern Tunisia: climatic or human impact? Quat. Sci. Rev. 23, 1757–1775.

Fedoroff, N., Courty, M.-A., 2013. Revisiting the genesis of red Mediterranean soils. Turk. J. Earth Sci. 22, 359–375.

Fletcher, W.J., Zielhofer, C., 2013. Fragility of western Mediterranean landscapes during Holocene rapid climate changes. Catena 103, 16–29.

Folk, R.L., Ward, W.C., 1957. Brazos River bar: a study in the significance of grain size parameters. J. Sediment. Petrol. 27, 3–26.

Galbraith, R.F., 2005. Statistics for Fission Track Analysis. Chapman & Hall/CRC, Boca Raton.

Galbraith, R.F., Green, P.F., 1990. Estimating the component ages in a finite mixture. Nucl. Tracks Radiat. Meas. 17 (3), 197–206.

Galbraith, R.F., Roberts, R.G., Laslett, G.M., Yoshida, H., Olley, J.M., 1999. Optical dating of single and multiple grains of quartz from Jinmium rock shelter, northern Australia: part I, experimental design and statistical models. Archaeometry 41 (2), 339–364.

García-García, F., Calero, J., Pérez-Valera, F., 2016. Morphological, pedological, and sedimentary evolution on the fringe of the southwestern European drylands during the late Pleistocene and Holocene: evidence of climate and land use changes. Catena 143, 128–139.

Guérin, G., Mercier, N., Adamiec, G., 2011. Dose-rate conversion factors: update. Ancient TL 29, 5–8.

Guérin, G., Mercier, N., Nathan, R., Adamiec, G., Lefrais, Y., 2012. On the use of the infinite matrix assumption and associated concepts: a critical review. Radiat. Meas. 47, 778–785.

Heiri, O., Lotter, A.F., Lemcke, G., 2001. Loss on ignition as a method for estimating organic and carbonate content in sediments: reproducibility and comparability of results. J. Paleolimnol. 25, 101–110.

Huntley, D.J., Baril, M.R., 1997. The K content of the K-feldspars being measured in optical dating or in thermoluminescence dating. Ancient TL 15 (1), 11–13.

Huntley, D.J., Lamothe, M., 2001. Ubiquity of anomalous fading in K-feldspars and the measurement and correction for it in optical dating. Can. J. Earth Sci. 38, 1093–1106.

Ibouhouten, H., Zielhofer, C., Mahjoubi, R., Kamel, S., Linstädter, J., Mikdad, A., Bussmann, J., Werner, P., Härtling, J.W., Fenech, K., 2010. Archives alluviales holocène et occupation humaine en Basse Moulouya (Maroc nord-oriental). Géomorphologie 16, 41–56.

IUSS Working Group WRB, 2014. World reference base for soil resources 2014. International Soil Classification System for Naming Soils and Creating Legends for Soil Maps. World Soil Resources Reports No. 106. FAO, Rome.

Jain, M., Murray, A.S., Bøtter-Jensen, L., 2004. Optically stimulated luminescence dating: how significant is incomplete light exposure in fluvial environments? Quaternaire 15 (1–2), 143–157.

Kars, R.H., Reimann, T., Ankjærgaard, C., Wallinga, J., 2014. Bleaching of the post-IR IRSL signal: new insights for feldspar luminescence dating. Boreas 43, 780–791.

Klasen, N., Hilgers, A., Schmidt, C., Bertrams, M., Schyle, D., Lehmkuhl, F., Richter, J., Radtke, U., 2013. Optical dating of sediments in Wadi Sabra (SW Jordan). Quat. Geochronol. 18, 9–16.

Komatsu, T., Tsukamoto, S., 2015. Late Glacial lake-level changes in the Lake Karakul basin (a closed glacierized-basin), eastern Pamirs, Tajikistan. Quat. Res. 83, 137–149.

Kreutzer, S., Schmidt, C., Fuchs, M.C., Dietze, M., Fischer, M., Fuchs, M., 2012. Introducing an R package for luminescence dating analysis. Ancient TL 30 (1), 1–8.

Li, B., Li, S.-H., 2012. A reply to the comments by Thomsen et al. on "Luminescence dating of K-feldspar from sediments: a protocol without anomalous fading correction". Quat. Geochronol. 8, 49–51.

Lindbo, D.L., Stolt, M.H., Vepraskas, M.J., 2010. Redoximorphic features. In: Stoops, G., Marcelino, V., Mees, F. (Eds.), Interpretation of Micromorphological Features of Soils and Regoliths. Elsevier, Amsterdam, pp. 129–147.

Linstädter, J., Eiwanger, J., Mikdad, A., Weniger, G.-C., 2012. Human occupation of Northwest Africa: a review of middle Palaeolithic to Epipalaeolithic sites in Morocco. Quat. Int. 274, 158–174.

Lubell, 2001. Late Pleistocene-early Holocene Maghreb. In: Peregrine, P.N., Ember, M. (Eds.), The Encyclopedia of Prehistory. 1, pp. 129–149 (Africa, Plenum, New York).

Macklin, M.G., Fuller, I.C., Lewin, J., Maas, G.S., Passmore, D.G., Rose, J., Woodward, J.C., Black, S., Hamlin, R.H.B., Rowan, J.S., 2002. Correlation of fluvial sequences in the Mediterranean basin over the last 200 ka and their relationship to climate change. Quat. Sci. Rev. 21, 1633–1641.

McGregor, H.V., Dupont, L., Stuut, J.-B.W., Kuhlmann, H., 2009. Vegetation change, goats, and religion: a 2000-year history of land use in southern Morocco. Quat. Sci. Rev. 28 (15–16), 1434–1448.

McLaren, 2004. Characteristics, evolution, and distribution of Quaternary channel calcretes, southern Jordan. Earth Surf. Process. Landf. 29, 1487–1507.

Mikdad, A., Moser, J., Ben-Ncer, A., 2002. Recherche préhistoriques dans le gisement d'Ifri n'Ammar au Rif Oriental (Maroc). Premiers résultats. Beiträge zur Allgemeinen und Vergleichenden Archäologie 22, 1–20.
Mikdad, A., Moser, J., Nami, M., Eiwanger, J., 2004. La stratigraphie du site Ifri n'Ammar (Rif Oriental, Maroc): premiers résultats sur les dépôts du Paléolithique moyen. Beiträge zur Allgemeinen und Vergleichenden Archäologie 24, 125–137.
Mook, D.H., Hoskin, C.M., 1982. Organic determinations by ignition: caution advised. Estuar. Coast. Shelf Sci. 15 (6), 697–699.
Moore, D.M., Reynolds, R.C., 1997. X-ray Diffraction and the Identification and Analysis of Clay Minerals. Oxford University Press, Oxford.
Moreno, A., 2012. A multiproxy paleoclimate reconstruction over the last 250 kyr from marine sediments: the northwest African margin and the western Mediterranean sea. In: Hublin, J.-J., McPherron, S.P. (Eds.), Modern Origins. A North African Perspective, Vertebrate Paleobiology and Paleoanthropology. Springer Science and Business Media, Heidelberg, New York, London.
Moreno, A., Cacho, I., Canals, M., Prins, M.A., Sánchez-Goñi, M.F., Grimalt, J.O., Weltje, G.J., 2002. Saharan dust transport and high-latitude glacial climatic variability: the Alboran Sea record. Quat. Res. 58, 318–328.
Moser, J., 2003. La Grotte d'Ifri n'Ammar, Tome 1, L'Ibéromaurusien. AVA-Forschungen Band 8. Linden Soft.
Murray, A.S., Wintle, A.G., 2000. Luminescence dating of quartz using an improved single-aliquot regenerative-dose protocol. Radiat. Meas. 32, 57–73.
Murray, A.S., Wintle, A.G., 2003. The single aliquot regenerative dose protocol: potential for improvements in reliability. Radiat. Meas. 37, 377–381.
Murray, A.S., Thomsen, K.J., Masuda, F., Buylaert, J.P., Jain, M., 2012. Identifying well-bleached quartz using the different bleaching rates of quartz and feldspar luminescence signals. Radiat. Meas. 47, 688–695.
Nami, M., Moser, J., 2010. La grotte d'Ifri n'Ammar. Le Paléolithique moyen. Forschungen zur Archäologie Außereuropäischer Kulturen vol. 9. Reichert Verlag, Wiesbaden.
Nash, D.J., Smith, R.F., 2003. Properties and development of channel calcretes in a mountain catchment, Tabernas basin, southeast Spain. Geomorphology 50, 227–250.
Nathan, R.P., Mauz, B., 2008. On the dose-rate estimate of carbonate-rich sediments for trapped charge dating. Radiat. Meas. 43, 14–25.
Patton, P.C., Schumm, S.A., 1981. Ephemeral-stream processes: implications for studies of Quaternary valley fills. Quat. Res. 15, 24–43.
Pérez-Folgado, M., Sierro, F.J., Flores, J.A., Grimalt, J.O., Zahn, R., 2004. Palaeoclimatic variations in foraminifer assemblages from the Alboran Sea (western Mediterranean) during the last 150 ka in ODP site 977. Mar. Geol. 212, 113–131.
Pissart, A., Boumeaza, T., 2010. Âge et origine de la terrasse limoneuse de la basse Moulouya (Maroc nord-oriental). Bulletin de la Société Géographique de Liège 54, 85–96.
Poesen, J.W.A., Hooke, J.M., 1997. Erosion, flooding and channel management in Mediterranean environments of southern Europe. Prog. Phys. Geogr. 21 (2), 157–199.
Prescott, J.R., Hutton, J.T., 1994. Cosmic ray contributions to dose rates for luminescence and ESR dating: large depths and long-term time variations. Radiat. Meas. 23, 497–500.
Preusser, F., Andersen, B.G., Denton, G.H., Schlüchter, C., 2005. Luminescence chronology of late Pleistocene glacial deposits in north Westland, New Zealand. Quat. Sci. Rev. 24, 2207–2227.
Reimann, T., Thomsen, K.J., Jain, M., Murray, A.S., Frechen, M., 2012. Single-grain dating of young sediments using the pIRIR signal from feldspar. Quat. Geochronol. 11, 28–41.
Richter, D., Moser, J., Nami, M., Eiwanger, J., Mikdad, A., 2010. New chronometric data from Ifri n'Ammar (Morocco) and the chronostratigraphy of the middle Palaeolithic in the western Maghreb. J. Hum. Evol. 59 (6), 672–679.
Rixhon, G., Briant, R.M., Cordier, S., Duval, M., Jones, A., Scholz, D., Revealing the pace of river landscape evolution during the Quaternary: recent developments in numerical dating methods, Quat. Sci. Rev., http://dx.doi.org/10.1016/j.quascirev.2016.08.016 (in press).
Rixhon, G., Bartz, M., El Ouahabi, M., Szemkus, N., Brückner, H., 2017. Contrasting terrace systems of the lower Moulouya river as indicator of crustal deformation in NE Morocco. J. Afr. Earth. Sci. 126, 45–57.
Sandercock, P.J., Hooke, J.M., Mant, J.M., 2007. Vegetation in dryland river channels and its interaction with fluvial processes. Prog. Phys. Geogr. 31 (2), 107–129.
Santisteban, J.I., Schulte, L., 2007. Fluvial networks of the Iberian peninsula: a chronological framework. Quat. Sci. Rev. 26, 2738–2757.
Schulte, L., 2003. River response and terrace agradation in the Mediterranean Iberian peninsula during historical times. In: Thorndycraft, V.R., Benito, G., Barriendos, M., Llasat, C. (Eds.), Palaeofloods, Historical Floods and Climatic Variability: Applications in Flood Risk Assessment (Proceedings of the PHEFRA Workshop, Barcelona, 16th–19th October, 2002).
Segura-Beltrán, F., Sanchis-Ibor, C., 2013. Assessment of channel changes in a Mediterranean ephemeral stream since the early twentieth century. The Rambla de Cervera, eastern Spain. Geomorphology 201, 199–214.
Snoussi, M., Haida, S., Imassi, S., 2002. Effects of the construction of dams on the water and sediment fluxes of the Moulouya and the Sebou rivers, Morocco. Reg. Environ. Chang. 3, 5–12.
Stoops, 2003. Guidelines for Analysis and Description of Soil and Regolith Thin Sections. Soil Science Society of America, Inc., Madison, Wisconsin.
Sutherland, 1998. Loss-on-ignition estimates of organic matter and relationships to organic carbon in fluvial bed sediments. Hydrobiologia 389, 153–167.
Thiel, C., Buylaert, J.P., Murray, A.S., Tsukamoto, S., 2011. On the applicability of post-IR IRSL dating to Japanese loess. Geochronometria 38, 369–378.
Thomsen, K.J., Murray, A.S., Jain, M., Bøtter-Jensen, L., 2008. Laboratory fading rates of various luminescence signals from feldspar-rich sediment extracts. Radiat. Meas. 43, 1474–1486.
Thomsen, K.J., Murray, A.S., Buylaert, J.P., Jain, M., Hansen, J.H., Aubry, T., 2016. Testing single-grain quartz OSL methods using sediment samples with independent age control from the Bordes-Fitte rockshelter (Roches d'Abilly site, central France). Quat. Geochronol. 31, 77–96.
Tjallingii, R., Claussen, M., Stuut, J.-B.W., Fohlmeister, J., Jahn, A., Bickert, T., Lamy, F., Röhl, U., 2008. Coherent high- and low-latitude control of the northwest African hydrological balance. Nat. Geosci. 1, 670–675.
USGS, 2015. NASA EOSDIS Land Processes Distributed Active Archive Center (LP DAAC). USGS/Earth Resources Observation and Science (EROS) Center, Sioux Falls, South Dakota.
Wallinga, J., 2002. Optically stimulated luminescence dating of fluvial deposits: a review. Boreas 31, 303–322.
Wintle, A., 1973. Anomalous fading of thermoluminescence in mineral samples. Nature 245, 143–144.
Wintle, A.G., Murray, A., 2006. A review of quartz optically stimulated luminescence characteristics and their relevance in single-aliquot regeneration dating protocols. Radiat. Meas. 41, 369–391.
Wolf, D., Faust, D., 2015. Western Mediterranean environmental changes: evidences from fluvial archives. Quat. Sci. Rev. 122, 30–50.
Wolf, D., Seim, A., Faust, D., 2014. Fluvial system response to external forcing and human impact – late Pleistocene and Holocene fluvial dynamics of the lower Guadalete River in western Andalucía (Spain). Boreas 43, 422–429.
Zielhofer, C., 2007. Climate change and landscape-ecological effects in the western Mediterranean – future, present and learning from the past. Eur. Reg. 15 (2), 110–118.
Zielhofer, C., Linstädter, J., 2006. Short-term mid-Holocene climatic deterioration in the west Mediterranean region: climatic impact on Neolithic settlement pattern? Z. Geomorphol. N.F. 142, 1–17.
Zielhofer, C., Faust, D., Baena Escudero, R., Diaz del Olmo, F., Kadereit, A., Moldenhauer, K.-M., Porras, A., 2004. Centennial-scale late-Pleistocene to mid-Holocene synthetic profile of the Medjerda Valley, northern Tunisia. The Holocene 14 (6), 851–861.
Zielhofer, C., Faust, D., Linstädter, J., 2008. Late Pleistocene and Holocene alluvial archives in the southwestern Mediterranean: changes in fluvial dynamics and past human response. Quat. Int. 181, 39–54.
Zielhofer, C., Bussmann, J., Ibouhouten, H., Fenech, K., 2010. Flood frequencies reveal Holocene rapid climate changes (lower Moulouya River, northeastern Morocco). J. Quat. Sci. 25 (5), 700–714.